



UNIVERSITÀ  
DEGLI STUDI  
DI PADOVA

UNIVERSITA' DEGLI STUDI DI PADOVA

**Dipartimento di Ingegneria Industriale DII**

Corso di Laurea Magistrale in Ingegneria dell'Energia Elettrica

**Misure su motore a magneti permanenti interni a flusso intensificato per  
un controllo ottimale di coppia**

Relatore: Prof. Silverio Bolognani

Supervisore: Prof. Marko Hinkkanen

Laureando: Andrea Comin

1132742

Anno Accademico 2017/2018

Copyright © 2018 Andrea Comin

---

**Author** Andrea Comin

---

**Title** Measurements on a flux intensifying interior permanent magnet motor for an optimal torque control

---

**Degree programme** Electrical Power and Energy Engineering

---

**Major** Electric Drives

**Code of major** ELEC-E8405

---

**Supervisor and advisor** Professor Marko Hinkkanen

---

**Date** 6.7.2018

**Number of pages** 75

**Language** English

---

**Abstract**

The aim of this final project elaborated at "University of Padova" and at "Aalto University" is to determine the parameters that characterize the behavior of the flux intensifying interior permanent magnet motor and to study the reference calculations in order to implement suitable lookup tables in a Simulink sensorless model. In the first part of the work a series of tests have been carried out in order to collect data related to the motor developed by the team of Edlab in Padova. The description of the test benches, the used software and the obtained results are reported in the first chapters which are dedicated to the measurements. Thanks to the tests carried out on the bench for slow speed it has been possible to collect the data about the trends of the cogging torque, of the torque as function of the angle of the current and of the torque in MTPA (maximum torque per ampere) conditions. Furthermore the mapping of the torque has been obtained. The tests carried out on the bench for high speed have been used to achieve a map of the flux and a second map of the torque which has been used to check the correctness of the results obtained with the tests on the bench for slow speed. In order to extrapolate the information relative to the fluxes a method has been used which permits the knowledge of the resistance to be avoided. This method consists of two tests, the first at  $(I_d, I_q)$  and the second at  $(I_d, I_q)$ . If the two tests are carried out in a relatively short temporal range, the resistance value can be considered unvaried and this aspect has been used to solve the system of equation which has been used for the test. The second part is dedicated to the achievement of lookup tables. Using an algebraic magnetic model it has been possible to use the collected data for the realization of the lookup tables which replace an operation of computation with a simpler indexing operation and consequently retrieving a value from the memory. This can save significant processing time. At the end, the lookup tables have been implemented in a Simulink sensorless model in order to realize the simulation to evaluate the correctness of the reference calculations. The achieved results have confirmed the quality of the fitting and of reference calculations.

---

**Keywords** measurements , torque control , flux intensifying interior permanent magnet

---

# Index

<b>1</b>	<b>Introduction and thesis statement</b>	<b>9</b>
1.1	State of the art . . . . .	9
1.1.1	Rated current and operations at high speed . . . . .	9
1.1.2	Cross saturation and self-sensing performance . . . . .	11
1.1.3	IPM vs FI-IPM . . . . .	12
1.1.4	Previous work . . . . .	13
1.2	Aim . . . . .	14
<b>2</b>	<b>The motor IPM-FI</b>	<b>15</b>
2.1	Structure . . . . .	15
2.2	Equations of an IPM motor . . . . .	16
2.3	Limits and operating regions . . . . .	18
2.3.1	IPM, $C$ is external . . . . .	19
2.3.2	IPM, $C$ is internal . . . . .	21
2.3.3	IPM-FI, $C$ is external . . . . .	22
2.3.4	IPM-FI, $C$ is internal . . . . .	22
2.4	Data . . . . .	23
2.4.1	Performance Data . . . . .	23
2.4.2	Windings . . . . .	23
2.4.3	Results obtained by previous FEA tests . . . . .	24
<b>3</b>	<b>Motor Measurements</b>	<b>26</b>
3.1	Magnetic saturation and cross coupling effect . . . . .	26
3.1.1	Magnetic saturation . . . . .	26
3.1.2	Cross coupling effect . . . . .	26
3.2	Test bench for slow speeds . . . . .	27
3.2.1	Software . . . . .	29
3.2.2	Cogging torque . . . . .	30
3.2.3	Torque as a function of $\alpha_{ie}$ . . . . .	34
3.2.4	Mapping . . . . .	35
3.2.5	Torque in MTPA condition . . . . .	37
3.3	Test bench for fast speeds . . . . .	40
3.3.1	Software . . . . .	42

---

3.3.2	Mapping of flux and torque . . . . .	43
3.3.3	Results . . . . .	46
3.4	Back emf . . . . .	52
<b>4</b>	<b>Electric drive</b>	<b>54</b>
4.1	Motor model . . . . .	54
4.2	Algebraic magnetic model and fitting . . . . .	55
4.2.1	Fitting using a polynomial function . . . . .	56
4.2.2	Aalto fitting tool . . . . .	60
4.3	MTPA and MTPV locus . . . . .	63
4.4	Lookup tables . . . . .	65
4.5	Control system . . . . .	67
4.6	Simulations . . . . .	67
<b>5</b>	<b>Conclusions</b>	<b>70</b>
	<b>biblio</b>	<b>73</b>

# List of figures

2.1	Limits and operating regions of a IPM: $C$ external . . . . .	20
2.2	Characteristic torque-speed: $C$ external . . . . .	20
2.3	Limits and operating regions of a IPM: $C$ internal . . . . .	21
2.4	Characteristic torque-speed: $C$ internal . . . . .	21
2.5	Limits and operating regions of a IPM-FI: $C$ external . . . . .	22
2.6	Limits and operating regions of a IPM-FI: $C$ internal . . . . .	23
3.1	Main elements of the slow bench . . . . .	28
3.2	Cogging torque, 100 [Nm] full-scale . . . . .	31
3.3	Cogging torque, 5 [Nm] full-scale . . . . .	32
3.4	Zoomed view of the cogging torque . . . . .	33
3.5	Harmonic content of the cogging torque . . . . .	33
3.6	Torque as a function of $\alpha_{ie}$ . . . . .	34
3.7	Map 22 22, step 2[A] . . . . .	36
3.8	Map 15 15, step 1[A] . . . . .	36
3.9	Average torque in MTPA condition . . . . .	37
3.10	Torque in MTPA condition . . . . .	38
3.11	Harmonic content of torque operating in MTPA condition and at nominal current . . . . .	39
3.12	Main elements of the fast bench . . . . .	41
3.13	Measured torque map at fast bench . . . . .	46
3.14	Calculated (dashed lines) and measured torque map at fast bench . . . . .	47
3.15	d-axis flux . . . . .	47
3.16	q-axis flux . . . . .	48
3.17	q-axis flux, at $I_d = -20[A]$ , $I_d = 0[A]$ , $I_d = 20[A]$ , . . . . .	48
3.18	Flux map . . . . .	49
3.19	$L_d$ map . . . . .	50
3.20	$L_q$ map . . . . .	50
3.21	Saliency ratio map . . . . .	51
3.22	Back emf seen on oscilloscope . . . . .	52
3.23	Back emf . . . . .	53
3.24	Harmonic content back emf . . . . .	53

---

4.1	Three-dimensional fitting with a polynomial function, $d$ axis .	57
4.2	Three-dimensional fitting with a polynomial function, $q$ axis .	57
4.3	Two-dimensional fitting with a polynomial function, $d$ axis . .	58
4.4	Two-dimensional fitting with a polynomial function, $q$ axis . .	58
4.5	Two-dimensional fitting with a polynomial function omitting part of the coefficients, $d$ axis . . . . .	59
4.6	Two-dimensional fitting with a polynomial function omitting part of the coefficients, $q$ axis . . . . .	59
4.7	Three-dimensional fitting with Aalto's tool, $d$ axis . . . . .	61
4.8	Three-dimensional fitting with Aalto's tool, $q$ axis . . . . .	61
4.9	Two-dimensional fitting with Aalto's tool, $d$ axis . . . . .	62
4.10	Two-dimensional fitting with Aalto's tool, $q$ axis . . . . .	62
4.11	Reference calculations scheme . . . . .	63
4.12	Circle diagram: MTPA locus (black), MTPV (green), voltage limit (blue) and the current limit (red) . . . . .	64
4.13	MTPA locus, MTPV and current limit . . . . .	65
4.14	Feasible operating region . . . . .	66
4.15	MTPA, MTPV and current limit in $i_d, i_q$ plane . . . . .	66
4.16	Trend of the torque . . . . .	68
4.17	Trend of the speed . . . . .	68
4.18	Trend of variables under control . . . . .	69
4.19	Position error . . . . .	69

# List of tables

2.1	Performance data . . . . .	23
2.2	Windings . . . . .	24
2.3	FEA results in MTPA conditions . . . . .	25
3.1	Torque as a function of $\alpha_{ie}$ . . . . .	35
4.1	Exponential coefficients of the algebraic model . . . . .	56
4.2	Fitting parameters using Aalto's tool . . . . .	60



## Chapter 1

# Introduction and thesis statement

The interior permanent magnet (IPM) motors have been studied for years by researchers since this kind of machines is characterized by high power density and efficiency. In flux weakening conditions, the common IPM motors require a negative current along the  $d$  axis to induce a positive contribution to the reluctance torque. Because of the rare earth magnets, the production costs of the permanent magnet motors are higher than the induction motors and higher than the reluctance machines. This is one of the reasons why a special IPM machine has been proposed and studied in the last years. It can work at load conditions with a positive value of the reluctance torque that is obtained by a positive current along the  $d$  axis. This is possible because of the particularity of this machine, in which the q-axis inductance  $L_q$  is smaller than the d-axis inductance  $L_d$ . This aspect enables to prevent the demagnetization of the magnets. This type of machine is known as flux intensifying interior permanent magnet (FI-IPm) motors.

### 1.1 State of the art

In the following pages the main results, that have been reached for the FI-IPM up to now, are reported.

#### 1.1.1 Rated current and operations at high speed

In the last twenty years researches and studies were carried out. In many of them the goal was to identify a way to design the machine in order to get the desired saliency ratio. Therefore in this section a description of the state of the art and of the main results is reported.

One of the first publications, released in 1999, was written by professors Bianchi and Bolognani, [2]. In that paper a structure of the IPM motor was examined, showing how the flux barriers should be designed to improve the motor performance. The characteristic reverse saliency, that is the ratio between  $L_d$  and  $L_q$  greater than the unity, can be obtained by implementing a given number of flux barriers that must have a particular shape in order to obstruct the  $q$  axis heavily without affecting the  $d$  axis. The reluctance motors design is based on a similar concept. The simplest solution was to add one barrier along the interpolar axis, though this does not allow the saliency ratio to reach a high value. The second possibility was characterized by the addition of four extra flux barriers per pole. As it was demonstrated by professors Bianchi and Bolognani, the position and the shape of the flux barriers are crucial not only for the saliency ratio, but also for the optimization of the torque ripple. The finite element analysis was used to compare the two solutions with a classic IPM. In the analysis both the permanent magnets and the stator configuration were not modified while modifying the rotor structure. As a result of this study, it was shown that the flux density at the air-gap, produced by the permanent magnet, is not affected by the flux barriers. Furthermore the flux density at the air-gap due to the current along the  $d$  axis is not modified by the interpolar barrier, but a small reduction was observed introducing the additional flux barriers. Vice versa the flux density at the air-gap due to the current along  $q$  axis is especially affected by the additional barriers. In the same analysis it was highlighted that the flux along the  $q$  axis decreases, adding the flux barriers, while for the  $d$  axis flux the variation is moderate and can only be observed for high value of  $d$  current. An operation point that seldom is used. In addition, a series of tests were carried out to evaluate the mechanical characteristics of the three different motors. Consequently it can be affirmed that below the base speed, the FI-IPM delivers a smaller torque than the one produced by the classic IPM. In the flux weakening area the roles are turned and this is due to a smaller  $L_q$ , which allows the same current vector to be kept by the drive up to a higher speed. The main contribution of this study was to confirm that the FI-IPM presents higher maximum speed and higher torque to current ratio than a normal IPM.

In 2000 an article produced by the same authors, Bianchi and Bolognani, was published [2]. In it an innovative design was investigated and compared with a classic one. In particular, the role of the saliency ratio and its influence on the other parameters were taken into account as well as the maximum feasible flux weakening speed and current vector control characteristics, considering the same drive performance. As already mentioned in the previous article, the flux barriers are introduced into a surface mounted permanent magnet or an interior permanent magnet to obtain the desired

saliency ratio, although it is not the only way, in fact it is possible to adopt a two-part rotor [4]-[5]. In the paper was shown that a lower value of the flux produced by the magnet is necessary to reach higher flux-weakening performance. Furthermore the PM flux linkage of an IPM decreases when the saliency ratio decreases and at the base point, the motor results in a reluctance torque higher than the torque due to the magnets. In contrast to this kind of machine, in the FI-IPM the PM flux linkage decreases, although slightly, when the saliency ratio increases. This leads to a higher PM torque component at base point with a lower current. Generally it can be affirmed that the main inductance, that is  $L_d$  for the FI-IPM and  $L_q$  for the IPM, is higher in an IPM than in a FI-IPM. In fact the associated flux to the main inductance crosses the air-gap and the magnets in a FI-IPM, whereas it crosses the air-gap twice in a IPM. A lower main inductance allows a faster current dynamic. Another important aspect that was underlined is the possibility of the FI-IPM motors to operate at higher maximum speed, and it increases with the saliency ratio and with the required flux weakening capabilities. It was also pointed out that the variation of the current vector angle from the base point to flux weakening point is larger and this allows the usage of encoders with a lower resolution.

### 1.1.2 Cross saturation and self-sensing performance

The cross saturation impact on the IPM machines and its consequently effect on sensorless drives was the central point of researches in studies like [9]-[11]. The sensorless ac drives allow the reduction of the costs and the sensors cabling and thanks to their increasing reliability this technology has been used for a wide class of applications. Unfortunately the cross saturation can lead to important errors on the estimation of the position, which is based on the differential anisotropy of the system. In the technical literature many options for the excitation have been proposed, like several types of carrier signals and modified PWM patterns. Rotating or pulsating vectors have been tested as well as the injection of both current and voltage signals. The flux-current characteristic is for a general IPM far from being linear and both saturation and cross saturation affect the motor anisotropy. This causes difficulties in the detection of the rotor position based on the signal injections. In the analysis carried out in the paper a small-signal linearized model was considered. This was necessary due to the small flux and current oscillation at the injected carrier frequency. Introducing a rotating voltage vector, having a given carrier pulsation, the presence of an error on the angle estimation due to the cross saturation was shown. A similar problem was observed when using a sinusoidal pulsating voltage. The error is variable and its magnitude depends on the differential inductance and thus on the working point. Consequently also the estimation of the position is affected by the working point. In the conclusions, the researchers affirm that the

resulting error is mostly due to the machine magnetic behavior than the signal injection strategy. The error can reach some tenths of degrees and a suitable compensation is necessary for accurate control actions. It was also affirmed that the effect of the cross-saturation causes less problems in the FI-IPM.

Even though is not part of this thesis it is important to bear in mind that many additional studies have been carried out on self-sensing performance at slow speed based on saliency tracking with high-frequency rotating vector carrier signal injection methods, [14]-[13]. In the cited references the superiority of the FI-IPM to the IPM was shown. In addition, a lower harmonic distortion and a smaller saliency angular offset were observed, [12] and [13].

### 1.1.3 IPM vs FI-IPM

One of the most interesting works done about FI-IPM is [8]. The paper proposes a rotor design that allows a better performance for self-sensing control at zero/very slow speed based on saliency tracking methods. A FI-IPM structure was developed as well as one conventional IPM having similar torque-speed capability. This was done in order to proceed to a fair evaluation and comparison of the performances. The FI-IPM is built on a baseline IPM design and the magnet volume in it is slightly smaller than in the base IPM. Therefore also the magnet flux linkage is slightly reduced. A weakness of this study is that these inductances are evaluated with the injection in the corresponding axis individually and this might not represent the real inductances during a load conditions where the machine is fed by both currents. Fundamental aspects of the machine like the torque production, the efficiency and the power conversion capabilities were investigated. As known the maximum torque per ampere current vector control is used to minimize copper losses and it was underlined that for the proposed FI-IPM the rated torque is lower than the baseline type, because of the lower magnetic material. The FI-IPM machine can operate both in flux intensifying and in flux weakening conditions, while the conventional IPM has a working area that is restricted to the flux weakening. In a FI-IPM having a saliency ratio slightly higher than the unity, just a small positive quantity of current along the  $d$  axis is necessary to work in a constant torque region. When the machine operates with a positive  $i_d$  it gains the contribution of the reluctance torque. When a higher speed is required and the voltage limit is reached, the current vector has to move towards the second quadrant to work in flux weakening condition to further suppress the induced voltage. In this condition the reluctance torque becomes negative though the produced torque by the FI-IPM is still higher than the one produced by the IPM and this is due to a larger  $i_q$ . The magnetic saturation has an important role in the power conversion capability of the machine. The conventional IPM motors can lose saliency

and reluctance torque and this leads to more complex control structures. In a IPM motor, generally, both inductances are really sensitive to the load current, mainly to the  $i_q$ . It was pointed out that the saliency changes quickly when the load increases. When operating in MTPA condition, the current vector is close to the  $q$  axis since the reluctance torque is small, but when the load increases the the current vector deviates in a position where the MTPA angle gives the maximum combination of both torque contributions. In the FI-IPM machine was demonstrated that the inductances are less affected by the increasing load. Because of the barriers,  $L_q$  is less sensitive to  $i_q$ . Consequently there is a reduced variation of the saliency. Furthermore the inductances do not suffer large variation over the load range and therefore the saliency does not decrease while feeding the motor with high currents. This non-decreasing saliency trend is important for the saliency-tracking self-sensing controls. In fact the limited variation of it allows the simplification of the decoupling and of the compensation methods and moreover allows the reliability results to be improved. Several experimental tests were carried out to compare the efficiency of the two typologies of motor, nonetheless it was done avoiding low speed and low torque conditions. From the obtained results, it can be affirmed that the FI-IPM machine can have comparable power conversion to the used baseline IPM. The article continues comparing the self-sensing capabilities at very low speed. A high-frequency rotating vector carrier signal injection has been implemented. First of all a high frequency machine model in  $dq$  reference frame was presented. Applying a rotating vector carrier voltage, it was possible to evaluate the resulting high-frequency current. A term of the resulting currents contains the information about the rotor position. An angular offset is present and this is due to high frequency resistance and the cross-saturation effect, which also causes a variation between the real current amplitude and the analytic evaluation. It was crucial to keep the error in an acceptable range in order to avoid too complex decoupling and compensation schemes. The FI-IPM machine has a flatter magnitude of the differential inductance over the entire load range, whereas in the IPM it decreases at high load conditions. In other words, the saturation effects can easily damage the saliency of the IPM.

#### 1.1.4 Previous work

This work is a natural extension of the thesis [23]. Therefore some points that were already studied and evaluated are just sketched out here.

- the FI-IPM has a flux density at the air-gap at no-load conditions that presents a lower THD which allows a good reduction of the harmonics;
- the flux linkage at no load condition has an almost sinusoidal waveform;

- the cogging torque of a FI-IPM has a reduced value, if it is compared to an IPM having similar performance;
- the flux density at the stator teeth is reduced and consequently the related iron losses decrease.

## 1.2 Aim

The aim of this thesis elaborated at "Università Degli Studi di Padova" and at "Aalto University" is to determine the parameters that characterize the behavior of the flux intensifying interior permanent magnet motor and to create a suitable control model. In the first part of the work a series of tests have been carried out in order to collect data related to the motor developed by the team of Edlab in Padova. The description of the test benches, the used software and the obtained results are reported in the first chapters which are dedicated to the measurements. The second part is dedicated to the achievement of lookup tables which will be insert in a Simulink sensorless control system. The aim of the simulation is to evaluate the correctness of the reference calculation.

## Chapter 2

# The motor IPM-FI

In this chapter the characteristics of the motor FI-IPM will be reported. This machine is a particular case of interior permanent magnet synchronous motor, in fact it has a saliency ratio greater than 1 which differs substantially from the traditional IPM motors. A description of an IPM will be reported in the following sections. After it a description of how this peculiarity has been achieved and how it modifies the behavior of the motor will be presented.

### 2.1 Structure

The IPM is used for application in which a high level of performances is required. An IPM differs from a SPM in the anisotropy that characterizes its magnetic structure. The disposition of the magnets in an IPM can create a tangential or a radial magnetization. It is necessary to explain why a tangential magnetization has been chosen in the case in point. The first aim is to optimize the flux density wave form at the air-gap in no load conditions and the second one is to increase the power density. This is due to the flux per pole which is produced by two adjacent magnets. When designing accurately the motor geometry is possible to have:

$$= \frac{L_d}{L_q} > 1 \quad (2.1)$$

This allows to work with a positive  $I_d$ . In this way the magnets demagnetization is prevented and a positive value of the reluctance torque is earned. The reduction of  $L_q$  is the starting point to get  $> 1$ . The elements that contribute to achieve the target are:

- *Magnets* displaced in order to have a tangential magnetization;
- *Axis q barriers* that are flux barriers which obstruct the flux along q axis. These barriers shall contribute to the achievement of two objec-

tives: an increased value of  $L_q$  and a reduced presence of the torque ripple;

- *Flux barriers* are barriers that have three aims: to increase the saliency ratio, to optimize the flux density waveform at the air-gap at no load condition and to reduce the torque ripple;
- *A not uniform air-gap* that gives the same advantages of the flux barriers except for the variation of the saliency ratio.

## 2.2 Equations of an IPM motor

In this kind of motor the electromechanical conversion is due to the principles of the electrodynamic systems and of the reluctance systems. The torque is given by these contributes. The general equations that are valid without any hypothesis are the following.

$$\begin{aligned} u_a(t) &= R \cdot i_a(t) + \frac{d\lambda_a(t)}{dt} \\ u_b(t) &= R \cdot i_b(t) + \frac{d\lambda_b(t)}{dt} \\ u_c(t) &= R \cdot i_c(t) + \frac{d\lambda_c(t)}{dt} \end{aligned} \quad (2.2)$$

An equivalent form can be obtained multiplying the first equation by 1, the second by  $e^{j \cdot \frac{2 \cdot \pi}{3}}$  and the third by  $e^{j \cdot \frac{4 \cdot \pi}{3}}$ . In fact this allows to represent the relations in a stationary reference system as shown in the following equation.

$$\mathbf{u}^s = R \cdot \mathbf{i}^s + \frac{d\boldsymbol{\lambda}^s}{dt} \quad (2.3)$$

In the equations 2.4  $i_a, i_b$  and  $i_c$  are the currents which feed the three phases;  $\lambda_a(t)$ ,  $\lambda_b(t)$  and  $\lambda_c(t)$  are the magnetic flux linkages with each phase and  $R$  is the phase resistance. It has been assumed that this last value is equal for each phase. Considering the motor not affected by the saturation, the linearity of the system can be used to identify the contributes of the magnets and of the currents to the flux linkage.

$$\begin{aligned} \lambda_a(t) &= \lambda_{a,PM}(t) + \lambda_{a,i}(t) \\ \lambda_b(t) &= \lambda_{b,PM}(t) + \lambda_{b,i}(t) \\ \lambda_c(t) &= \lambda_{c,PM}(t) + \lambda_{c,i}(t) \end{aligned} \quad (2.4)$$

Considering a sinusoidal distribution of the stator windings and a suitable shaping of the magnets, the flux linkages can be considered to have a sinusoidal waveform as expressed in the equations 2.5.



$$\begin{aligned}
\lambda_{a,PM} &= \Lambda_{PM} \cdot \cos(\theta_{me}) \\
\lambda_{b,PM} &= \Lambda_{PM} \cdot \cos\left(\theta_{me} - \frac{2\pi}{3}\right) \\
\lambda_{c,PM} &= \Lambda_{PM} \cdot \cos\left(\theta_{me} - \frac{4\pi}{3}\right)
\end{aligned} \tag{2.5}$$

In this system  $\Lambda_{PM}$  represents the peak value of the flux linkage for each phase due to the presence of the magnets and  $\theta_{me}$  is the electric angle between the a phase axis and the axis due to the field produced by the permanent magnets. The homopolar component is not present and the flux can be represented by its space vector in the stationary reference system.

$$\boldsymbol{\lambda}_{PM}^s = \Lambda_{PM} \cdot e^{j\theta_{me}} \tag{2.6}$$

Being an anisotropic magnetic structure, the reluctance varies along the air-gap, therefore the auto and mutual inductances are functions of the rotor position.

$$\begin{aligned}
L_\alpha &= L_\alpha(\theta) \\
L_\beta &= L_\beta(\theta) \\
L_{\alpha,\beta} &= L_{\alpha,\beta}(\theta)
\end{aligned} \tag{2.7}$$

The inductances  $L_\alpha$  and  $L_\beta$  have oscillating values with a maximum and a minimum value that are equal to  $L_d$  and  $L_q$ . Moving from di  $\alpha$ -  $\beta$  system to  $d - q$  system it is possible to obtain the following system.

$$\begin{aligned}
u_d &= R \cdot i_d + L_d \cdot \frac{di_d}{dt} - \omega_{me} \cdot L_q \cdot i_q \\
u_q &= R \cdot i_q + L_q \cdot \frac{di_q}{dt} - \omega_{me} \cdot L_d \cdot i_d + \omega_{me} \cdot \Lambda_{PM}
\end{aligned} \tag{2.8}$$

A full explanation of the steps done to get this system is available in [?]. The expression of torque can be evaluated considering the powers.

$$\frac{3}{2} \cdot (u_d \cdot i_d + u_q \cdot i_q) = \frac{3}{2} \cdot R \cdot (i_d^2 + i_q^2) + \frac{3}{2} \cdot \frac{d}{dt}(W_{mg}) + \frac{3}{2} \cdot \omega_{me} \cdot \Lambda_{PM} \cdot i_q \tag{2.9}$$

Where

- $\frac{3}{2} \cdot (u_d \cdot i_d + u_q \cdot i_q)$  is the absorbed power.
- $\frac{3}{2} \cdot R \cdot (i_d^2 + i_q^2)$  are the joule losses.

- $\frac{3}{2} \cdot \frac{d}{dt}(W_{mg})$  represents the variation of the magnetic energy.
- $\frac{3}{2} \cdot \omega_{me} \cdot \Lambda_{PM} \cdot i_q$  is electric energy converted in mechanical energy.

Therefore the torque is:

$$T = \frac{3}{2} \cdot p \cdot [\Lambda_{PM} \cdot i_q + i_d \cdot i_q \cdot (L_d - L_q)] \quad (2.10)$$

## 2.3 Limits and operating regions

An interesting comparison between IPM and FI-IPM can be carried out considering the operating regions. For an unsaturated motor the voltage limit is described by an ellipse which is centered in C. Being inversely proportional to the speed, the voltage limit becomes more stringent when the speed increases. Below the base speed the torque is limited by the current limit and the FI-IPM motor operates with a positive  $I_d$ . In this working point there are the contributes of both magnetic and reluctance torque. Above the base speed, where the voltage limit is reached, the current  $I_d$  must decrease and then reverse. In this condition the contribute of the reluctance torque is negative but the magnetic torque is still higher than a similar IPM motor. This is due to a greater value of  $I_q$ . When the center of the family of ellipses, described by the voltage limit, is inside the current limit, the voltage-limited region is achieved. Operating the motor with rated voltage while the current vector decreases its amplitude in order to follow the curve that connects the points P and C. At point C the speed tends to infinite. If C is external from the current limit at the point, C corresponds to the maximum speed. It as been observed in [1] and [8] that below the base speed, the FI-IPM motor delivers a smaller torque than an IPM but the roles change when operating in the flux-weakening region. Considering a motor working in a steady state condition where the currents and the voltages have sinusoidal waveforms with constant values of frequency and of amplitude. In addition the value of speed is constant. Even  $U_d, U_q, I_d, I_q$  in the  $d - q$  system are constants.

The current limit is:

$$I_d^2 + I_q^2 \leq I_n^2 \quad (2.11)$$

The voltage limit is:

$$U_d^2 + U_q^2 \leq U_n^2 \quad (2.12)$$

where  $I_n, U_n$  are the modulus of the space vectors. The first term corresponds to the rms nominal value of the phase current and it is defined on the data sheet.

Considering the equations 2.9, neglecting the resistances and the equation 2.12, it is possible to get:

$$\left(\frac{L_q}{L_d} \cdot I_q\right)^2 + \left(I_d + \frac{\Lambda_{PM}}{L_d}\right)^2 \leq \left(\frac{U_n}{\Omega_{me} \cdot L_d}\right)^2 \quad (2.13)$$

The limit of current is a circumference on the plane, compare to that the limit of voltage expressed by 2.13 is a family of concentric ellipses where the centre is in  $C = \left(-\frac{\Lambda_{PM}}{L_d}; 0\right)$ . The curves for an IPM are reported in figure 2.1 and 2.3. There are two cases.

### 2.3.1 IPM, $C$ is external

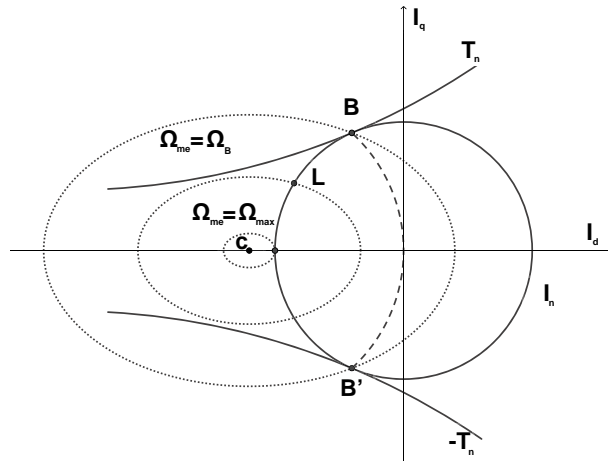
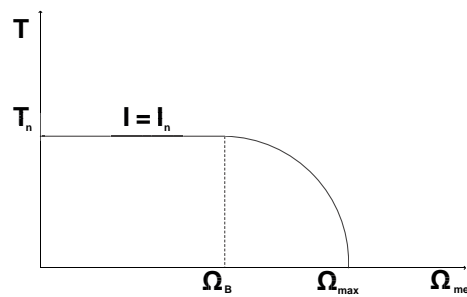
The first case is when the point  $C$  is external to the current limit circle. When the speed value is lower than  $\Omega_B$  it is possible to work on the MTPA (line  $BB'$ ). The points of the curve  $BB'$  are points where the torque hyperboles and the different current limits are tangential. Following the instruction defined in [?] the following equation has been obtained:

$$I_q = \frac{2 \cdot T}{3 \cdot 3} \cdot \frac{1}{\Lambda_{PM} + (L_d - L_q) \cdot I_d} \quad (2.14)$$

When the speed overcomes  $\Omega_B$  the operating point is  $L$ , which is the intersection between the limits. When the limits reach the point  $(-I_n; 0)$  the maximal speed is reached.

$$\Omega_{max} = \frac{U_n}{\Lambda_{PM} - L_d \cdot I_n} \quad (2.15)$$

The operating regions are reported in the figure 2.1 and the characteristic torque speed is reported in figure 2.2

Figure 2.1: Limits and operating regions of a IPM:  $C$  externalFigure 2.2: Characteristic torque-speed:  $C$  external

### 2.3.2 IPM, $C$ is internal

The first case is when the point  $C$  is internal to the current limit circle.

When the speed value is lower than  $\Omega_B$  it is possible to work on the MTPA (line  $BB'$ ), but when the speed overcomes  $\Omega_B$ , the operating point is  $L$  which is the intersection between the limits. This is valid up to the point where the torque hyperbole and the current limit are tangential,  $P$ . From there the working on the MTPV will be convenient. In this case there is not a maximum value of electrical speed because  $C$  is reached when  $\Omega_{me} \rightarrow \infty$ .

The operating regions are reported in the figure 2.3 instead the characteristic torque speed is reported in figure 2.4

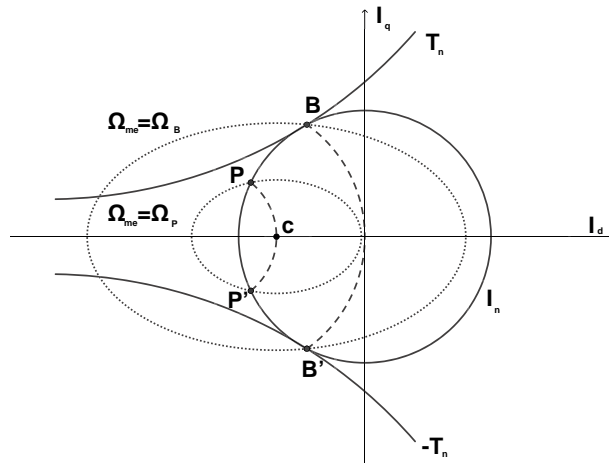


Figure 2.3: Limits and operating regions of a IPM:  $C$  internal

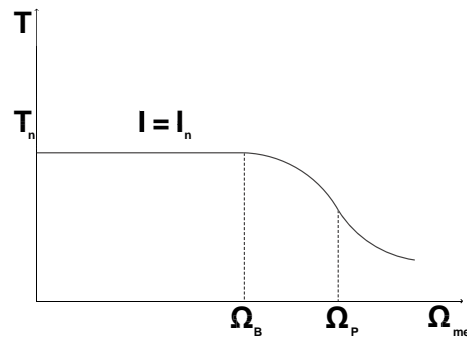
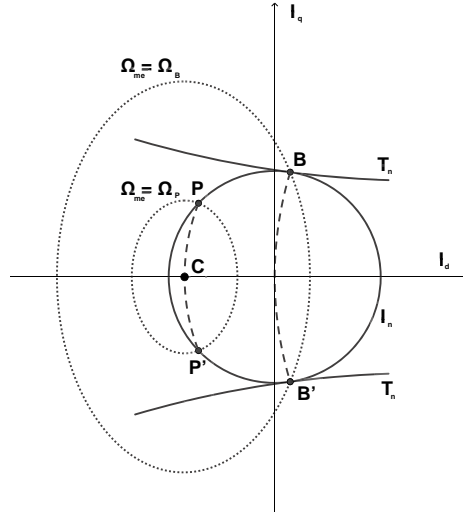


Figure 2.4: Characteristic torque-speed:  $C$  internal



Figure 2.6: Limits and operating regions of a IPM-FI: *C* internal

## 2.4 Data

In this section the data used to developed the motor are reported.

### 2.4.1 Performance Data

Performance Data			
Data	Symbol	Value	Unit of measure
Nominal power	$P_n$	4.8	[kW]
Nominal Torque	$T_n$	57.3	[Nm]
Current density	$J$	5.9	[A/mm <sup>2</sup> ]
Phase rms current	$I$	8.1	[A]
Phase rms voltage	$E$	202.2	[V]

Table 2.1: Performance data

### 2.4.2 Windings

The motor presents a single layer and not chorded winding, with a disposition of the wires which is represented by the winding matrix. The winding matrix represents the position of the winding in the stator slots. For each phase, the orientation of the current is marked and the presence of the phase in the slot is identified by a 1, instead the lack with a 0. Therefore the terms  $k_a$ ,

$k_b$  and  $k_c$  are the rows of the winding matrix and the columns of the matrix represent the slots.

$$k_a = \begin{matrix} 0 & 0 & 0 & 1 & 1 & 1 & 0 & 0 & 0 & 0 & 0 & 0 & -1 & -1 & -1 & 0 & 0 & 0 \\ 0 & 0 & 0 & 1 & 1 & 1 & 0 & 0 & 0 & 0 & 0 & 0 & -1 & -1 & -1 & 0 & 0 & 0 \end{matrix}$$

$$k_b = \begin{matrix} -1 & -1 & -1 & 0 & 0 & 0 & 0 & 0 & 0 & 0 & 1 & 1 & 1 & 0 & 0 & 0 & 0 & 0 & 0 \\ -1 & -1 & -1 & 0 & 0 & 0 & 0 & 0 & 0 & 0 & 1 & 1 & 1 & 0 & 0 & 0 & 0 & 0 & 0 \end{matrix}$$

$$k_c = \begin{matrix} 0 & 0 & 0 & 0 & 0 & 0 & -1 & -1 & -1 & 0 & 0 & 0 & 0 & 0 & 0 & 1 & 1 & 1 \\ 0 & 0 & 0 & 0 & 0 & 0 & -1 & -1 & -1 & 0 & 0 & 0 & 0 & 0 & 0 & 1 & 1 & 1 \end{matrix}$$

The winding data used in the realization of the motor is reported in the following table.

Winding Data			
Data	Symbol	Value	Unit of measure
Number of poles	$2p$	4	-
Number of phases	$m$	3	-
Number of slots	$Q_s$	36	-
Number of slots per pole and per phase	$q$	3	-
Angle of slot	$\alpha_s$	10	°
Electric angle of slot	$\alpha_{se}$	20	°
Periodicity	$t$	4	-
Coil throw	$Y_q$	9	-
Distribution coefficient	$k_d$	0.955	-
Chording coefficient	$k_r$	1	-
Winding coefficient	$k_w$	0.955	-
Number of series conductors per phase	$N_s$	456	-
Number of conductors in slot	$n_c$	38	-
Section of conductors	$S_c$	1.42	mm <sup>2</sup>
Number of elementary conductors	$n_{sc}$	2	-
Section of the elementary conductors	$d_c$	0.95	mm <sup>2</sup>
Fill factor	$k_{fill}$	0.47	-

Table 2.2: Windings

### 2.4.3 Results obtained by previous FEA tests

The results obtained in the previous thesis works are reported here.



Data	Symbol	Value	Unit of measure
Frequency	$f$	26.6	Hz
Speed	$n_n$	800	rpm
Nominal current	$I_n$	8.1	A
Direct synchronous inductance	$L_d$	55	mH
Synchronous inductance in quadrature	$L_q$	33	mH
Saliency ratio		1.8	-
Induction on stator tooth	$B_t$	1.83	T
Induction on stator backiron	$B_{bi}$	1.57	T
Stator joule losses	$P_{J,s}$	529	W
Stator teeth losses	$P_{fe,t}$	53	W
Stator backiron losses	$P_{fe,bi}$	91	W
Iron losses	$P_{fe}$	143	W
Mechanical losses	$P_m$	20	W
Total losses	$P_{loss}$	693	W
Efficiency		87.6	%

Table 2.3: FEA results in MTPA conditions

## Chapter 3

# Motor Measurements

The aim of this chapter is to get a complete characterization of the interior permanent magnet synchronous motor using measures of torque and flux. The measurements have been done on two test benches. The first, defined "slow bench", has been used to do measurements of the torque, whereas the second, named "fast bench", has been used to get information on the flux. A brief description of the benches, the procedures and of the used softwares will be presented in the following sections.

### 3.1 Magnetic saturation and cross coupling effect

In order to obtain a correct definition of the motor parameters it is important to bear in mind both the iron saturation and the cross-coupling effect.

#### 3.1.1 Magnetic saturation

The magnetic saturation causes the state which is reached when an increase of the applied external magnetizing field  $H$  cannot increase the magnetization of the material further. Magnetic materials like Iron and similars are composed of tiny regions named magnetic domains, that act like small permanent magnets and that can change their direction of magnetization. These domains are randomly oriented in absence of  $H$ , however the presence of an external magnetic field causes the alignment of the domains. Saturation is most clearly seen in the hysteresis curve, as a bending of the curve. As the  $H$  field increases, the  $B$  field approaches a maximum value asymptotically. Above saturation, the  $B$  field continues increasing, but at the paramagnetic rate.

#### 3.1.2 Cross coupling effect

The term cross-coupling refers to the effect of mutual interaction among the direct axis and the quadrature axis that occurs, when the motor is operating

in saturation condition. The flux produced by the current along the  $d$  or the  $q$  axis leads to saturation of parts of the machine, causing the distortion of the field lines on the other axis. Consequently we can write the following relations for the flux linkage.

$$\begin{aligned}\Lambda_d &= \Lambda_d(I_d, I_q) \\ \Lambda_q &= \Lambda_q(I_d, I_q)\end{aligned}\tag{3.1}$$

The equations (3.1) express the dependence of the fluxes on currents along both  $d$  axis and  $q$  axis. This effect will be presented and commented observing the graph 3.16.

## 3.2 Test bench for slow speeds

The slow bench used for the measures of torque is composed of:

- Master motor: three-phase brushless motor having a nominal power of 1.24 [kW] and a maximum speed of 3000 [rpm].
- Master inverter.
- Speed reducer with a reduction rate of 1/59.
- Slave motor: IPM-FI.
- Slave inverter.
- Steel structure.
- Mechanical seals.
- dSPACE DS1104.
- Computer.
- Cooling fan.
- Variable AC power supply for the slave inverter.
- DC power supply.
- Torque meter: 5 [Nm], 100 [Nm].
- Amplifier and filter for the signals of the torque meter.

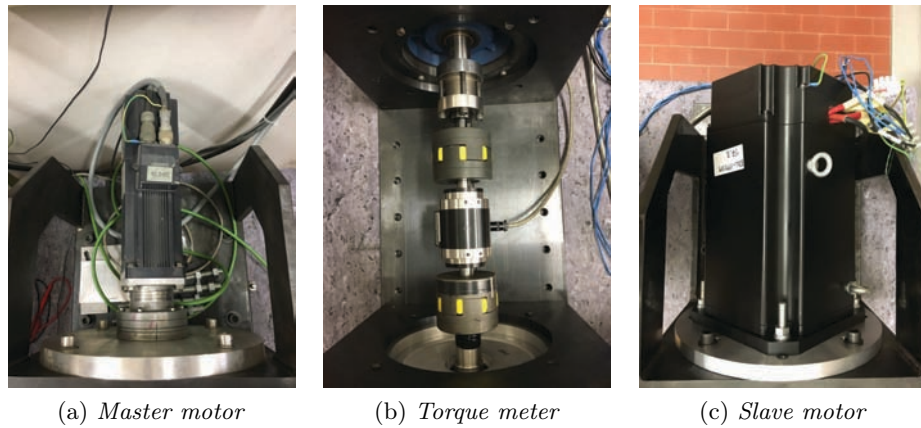


Figure 3.1: Main elements of the slow bench

The two test benches have a similar structure. The figure 3.1 represents the main elements of the slow bench. The adjustable supports, that can flow along the steel structure, allow both master and slave motors to be placed at the desired point, in order to satisfy the required distance from each other. Before every test, the supports must be anchored to the structure using screws. The connection between master and slave motor, rotating around the same axis, includes mechanical seals and a torque meter. The torque meter is connected to a filter and to an amplifier which provides a signal in the range  $0 - 5$  [V]. The signal is acquired and elaborated by the dSPACE board. Two torque meters have been used, one having 100 [Nm] as full-scale and the second is used to measure cogging torque with a full-scale of 5 [Nm]. Torque meters with lower values of full-scale are more precise but it is important not to go over the nominal torque value of the tool. The first reason is to avoid damages in the device, the second is that the values obtained over the nominal value cannot be trusted fully. The master motor has a speed reducer which allows to get high values of the torque in a low range of speed. Furthermore it gives the possibility to keep a constant speed of the master motor even when high variations of the torque occur. Considering the master parameters and the reducer, the slave motor can reach peak values of 50 [rpm] and 200 [Nm]. There are both a resolver and an incremental encoder (2048 [pulses/rpm]). The slave motor position is deduced knowing the one of the master. The motors are fed by two inverters with currents generated following the references offered by dSPACE board. The long duration of the tests required a cooling fan in order to keep the temperature of the slave motor under an acceptable limit and to avoid overheating.

### 3.2.1 Software

Softwares used for performing these tests are ControlDesk and Matlab. A brief explanation of the programs used is reported below.

#### 3.2.1.1 ControlDesk

A file with a *.cdx* extension contains and connects programs (*.c*) which define the interaction windows in order to visualize and modify variables. A file gets data and commands like pole number, motor speeds, full-scale of the used torque meter, activation and deactivation of the inverters and magnitude of the current. This file provides the mechanical position obtained by the encoder and the values of the torque achieved by the torque meter to MATLAB. Furthermore the file provides the reference currents as outputs of dSPACE.

#### 3.2.1.2 MATLAB

Several scripts have been used to carry out the different tests.

- The script for the evaluation of the cogging torque. The user must set in the program the installed torque meter, the pair pole number and the speed factor. During the test, MATLAB saves the torque values and the mechanical position, in a 62893 x 2 matrix.
- Another script is used to get torque values in MTPA condition while the motor is fed with synchronous currents. As previously explained it is necessary to set the initial parameters.

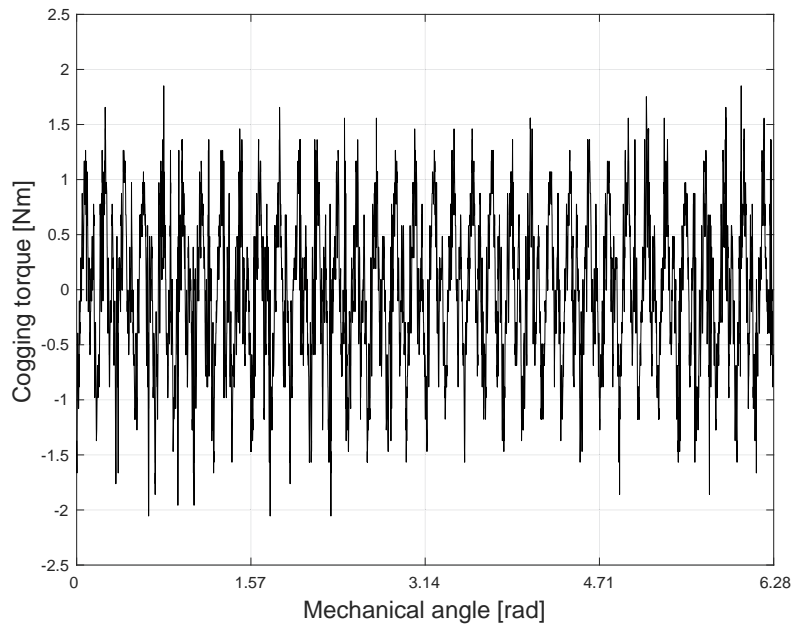
There is a first crucial part in which the system understands where the *d* and *q* axes are. To get this information the motor is fed with a constant current. The torque and position values are collected and inserted into a matrix. An elaboration of this data using Fourier analysis allows to identify the first harmonic. The *q* axis is located where the first harmonic of the torque has its peak and the *d* axis is placed where the first harmonic changes its sign. Because the first harmonic crosses the zero not in just one point, the *d* axis is determined considering the *q* axis position and then subtracting 90°. After that, the motor is fed with the current set at the beginning of the script.

- A script which follows the same procedure just described above is used in order to identify the position of *d* and *q* axes. The user sets a variation of angles between the currents along the *d* and the *q*. Observing the data collected, the angle where the MTPA condition is reached can be found. This test has been repeated for several current values.

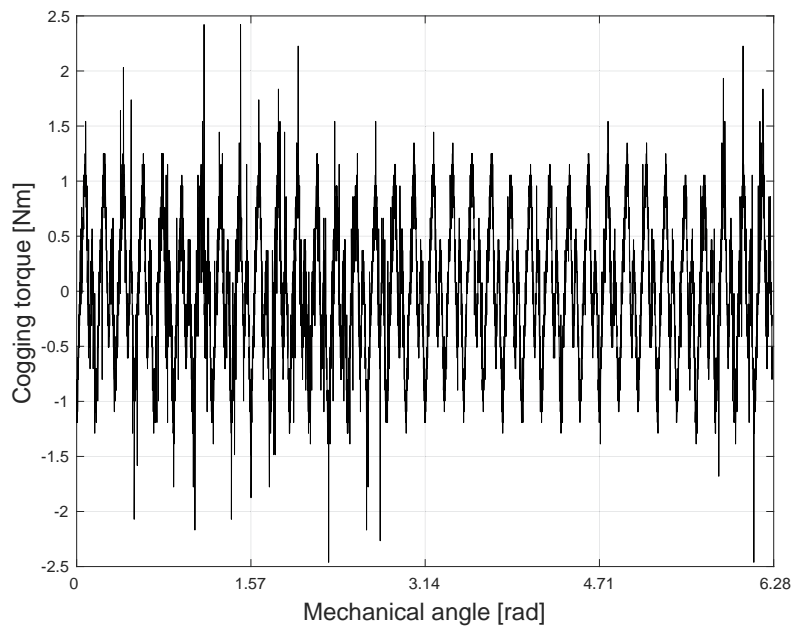
- At the end there is the procedure followed in order to collect data to realize a map of the motor. This is obtained varying the values of the current along the  $d$  and the  $q$  axis with a step defined by the user. A software protection has been implemented to avoid dangerous values of currents in the motor. In this case this fixed limit is 25A.

### 3.2.2 Cogging torque

Cogging torque is the value of torque obtained when the slave inverter does not feed the motor and the rotation is due to the master motor and in this case it is done at constant speed of 1 [rad/s]. The collected values show a clear dependence on both the pole number of the rotor and the stator slots. This effect can be noticed manually forcing a rotation of the shaft. In fact the rotor tends to place itself in order to get low reluctance paths causing a jerky rotation. Several tests are carried out, using a 100 [Nm] full-scale torque meter and a 5 [Nm] full-scale torque meter. It is important to operate with a constant speed in order to collect optimal results avoiding inertial torque contribution. Considering this aspect, tests with a reduced speed of 0.1 [rad/s] have been realized. Figure 3.3(b) represents the trend of the cogging evaluated with a torque meter having 100 [Nm] as full-scale and with a reduction speed factor equal to 10. As it can be observed comparing the figures, in this figure the values are in the range  $-1.5 - 1.5$  [Nm]. This trend is due to the use of a more accurate instrument. Figure 3.4 shows a zoomed view of the cogging torque. To complete this section, 3.5 displays the harmonic content. As mentioned before, the harmonic peak can be detected corresponding to the 36th harmonic.

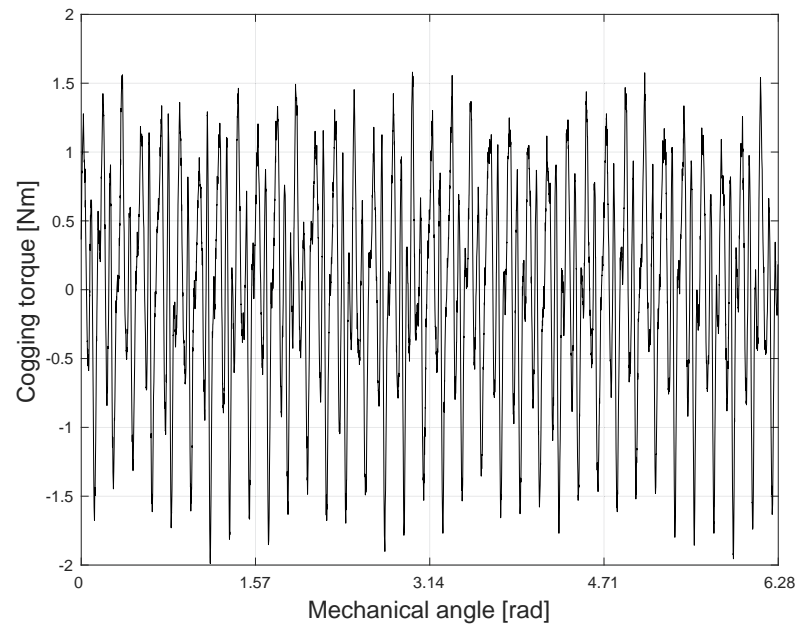


(a) at 1 [rad/s]

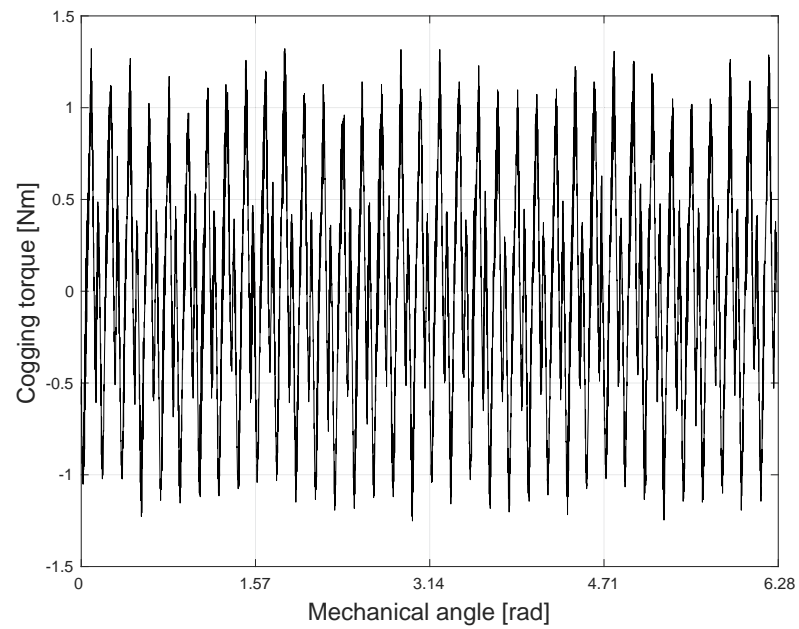


(b) at 0.1 [rad/s]

Figure 3.2: Cogging torque, 100 [Nm] full-scale



(a) at 1 [rad/s]



(b) at 0.1 [rad/s]

Figure 3.3: Cogging torque, 5 [Nm] full-scale



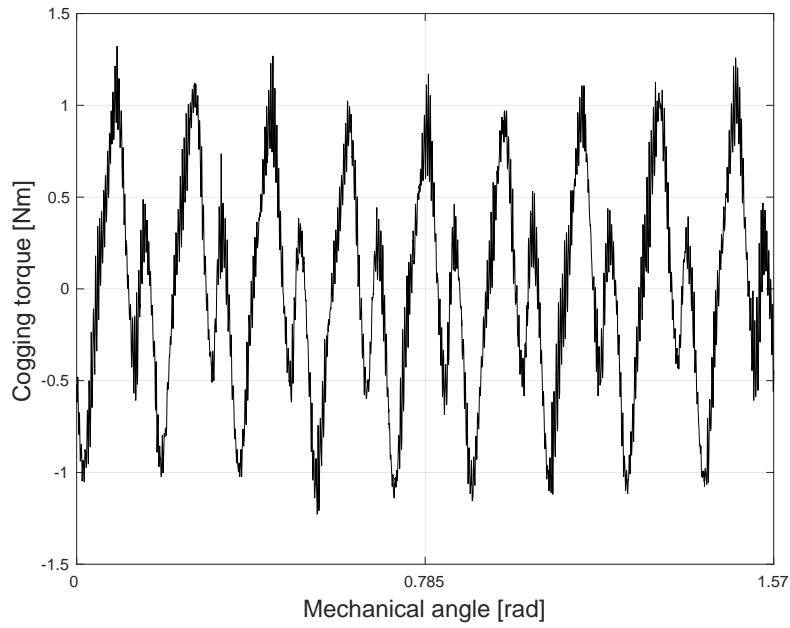


Figure 3.4: Zoomed view of the cogging torque

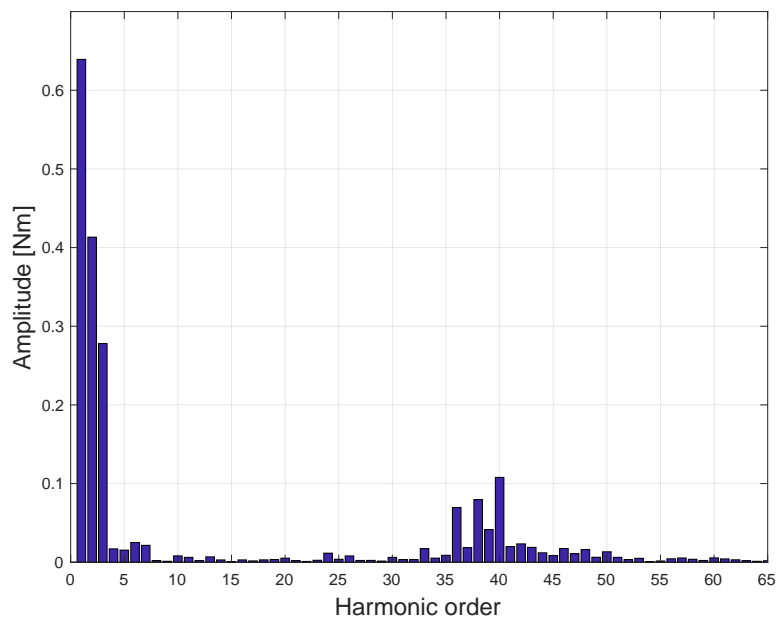


Figure 3.5: Harmonic content of the cogging torque

### 3.2.3 Torque as a function of $\alpha_{ie}$

For this test the slave motor is fed with a current set by the user. Varying the angle of the current vector the software collects torque values. An elaboration of the data saved by MATLAB allows the identification of the angle where the MTPA condition is reached. In first approximation the angle is varied with a step of  $5^\circ$ . Observing the collected data, the angle where the torque peak is reached can be identified and a second test is done varying the angle with a step of  $1^\circ$  around that value. These tests have been carried out for an array of values from  $0.25 \cdot I_n$  to  $2 \cdot I_n$  at a step of  $0.25[A]$ . In 3.6 in blue is plotted the curve due to  $I_n$  while the others refer to different values of current. It is important to remark the behavior of the motor while it is fed with a current which overcomes  $1.5 \cdot I_n$ .

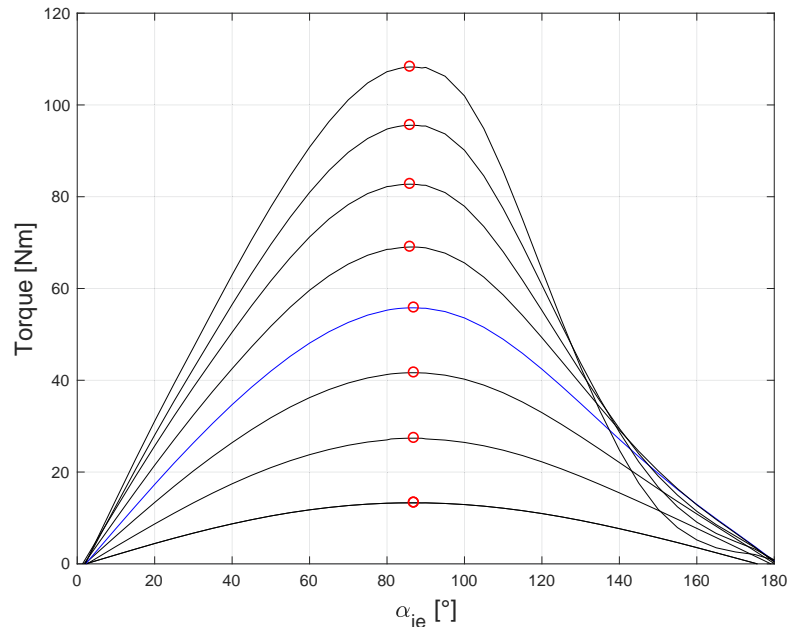


Figure 3.6: Torque as a function of  $\alpha_{ie}$

On the right part of the plot it can be noted that despite a higher value of the current, we obtain a lower value of torque. This behavior can be explained considering that the motor is no longer operating in MTPA condition. In conclusion the optimal  $\alpha_{ie}$  found are reported in the following table:

Current [A]	$\alpha_{ie}$ [°]
2.85	87
5.71	87
8.59	87
11.50	87
14.30	86
17.19	86
20.0	86

Table 3.1: Torque as a function of  $\alpha_{ie}$ 

### 3.2.4 Mapping

This test allows to define the contour map of the torque in a  $I_d, I_q$  plan. Several tests have been done, varying the map border and the steps of the current. In figure 3.7 a complete map obtained with current values from  $-22[A]$  to  $22[A]$  and with a step of  $2[A]$  for both  $I_d$  and  $I_q$  is shown. The white areas on the map are due to the lack of data, in fact some measures have not been done in order to avoid over-limits. A more detailed map, visible in figure 3.8 has been gained setting a step of  $0.5[A]$ . In this case the simulation could not have been carried out up to end and that has been caused by the shared memory limit between MATLAB and ControlDesk. This is why only the most interesting part of the map has been reported. The nominal current circumference and the MTPA curve have been drawn for both maps.

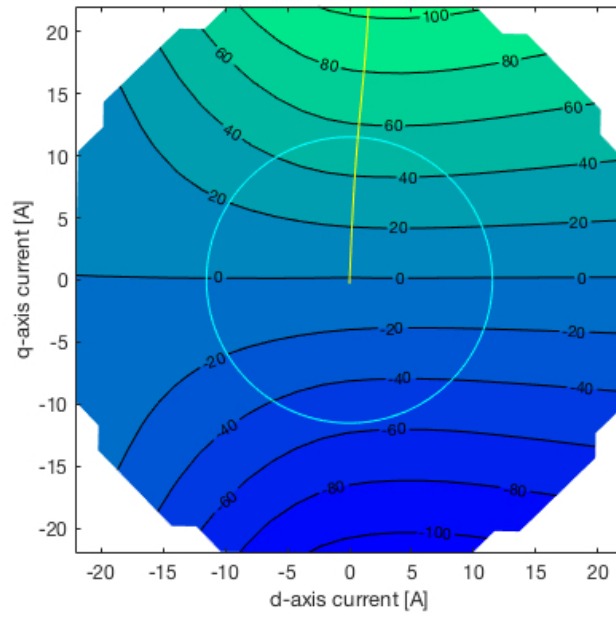


Figure 3.7: Map 22 22, step 2[A]

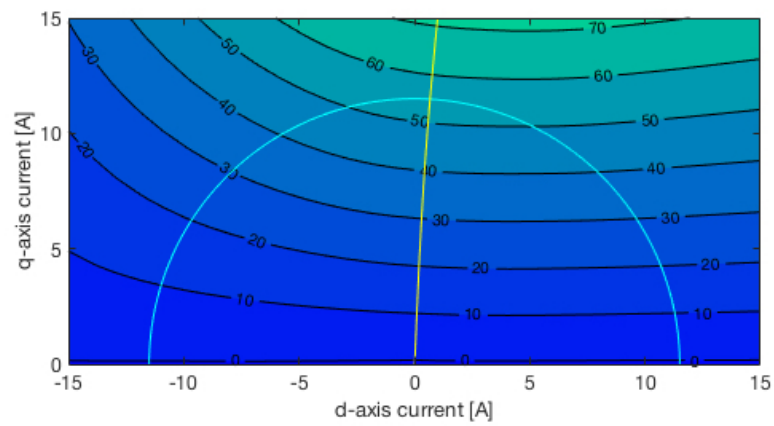


Figure 3.8: Map 15 15, step 1[A]

### 3.2.5 Torque in MTPA condition

In this part of the measurements done on the slow bench, the trend of the torque working in MTPA condition is reported in the figure 3.9 where the average value of the torque for each value of the current has been calculated in order to show the trend of the torque while the motor is working under MTPA conditions.

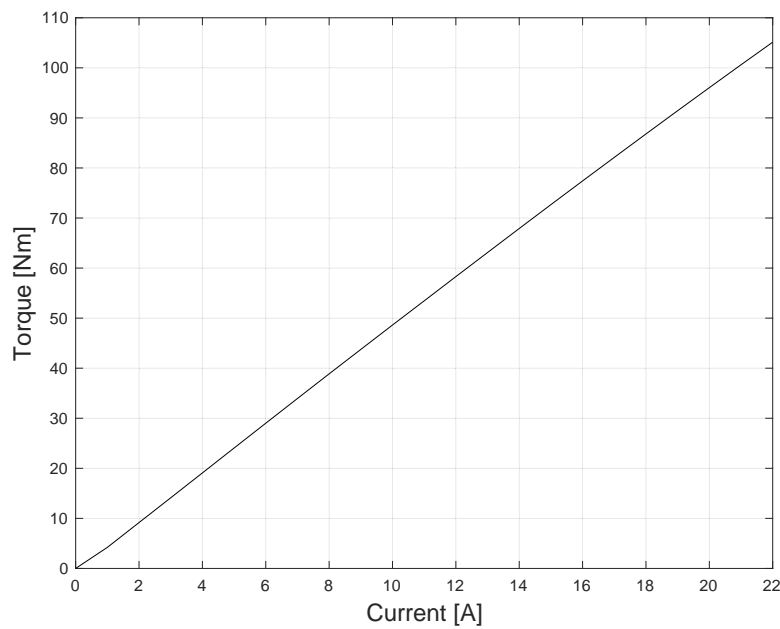


Figure 3.9: Average torque in MTPA condition

In figure 3.10 the trend of the torque for an array of current values from  $0.5 \cdot I_n$  to  $1.25 \cdot I_n$  with a step of  $0.25[A]$  has been reported. In figure 3.11 the harmonic content of the torque in MTPA condition at  $I_n$  can be observed.

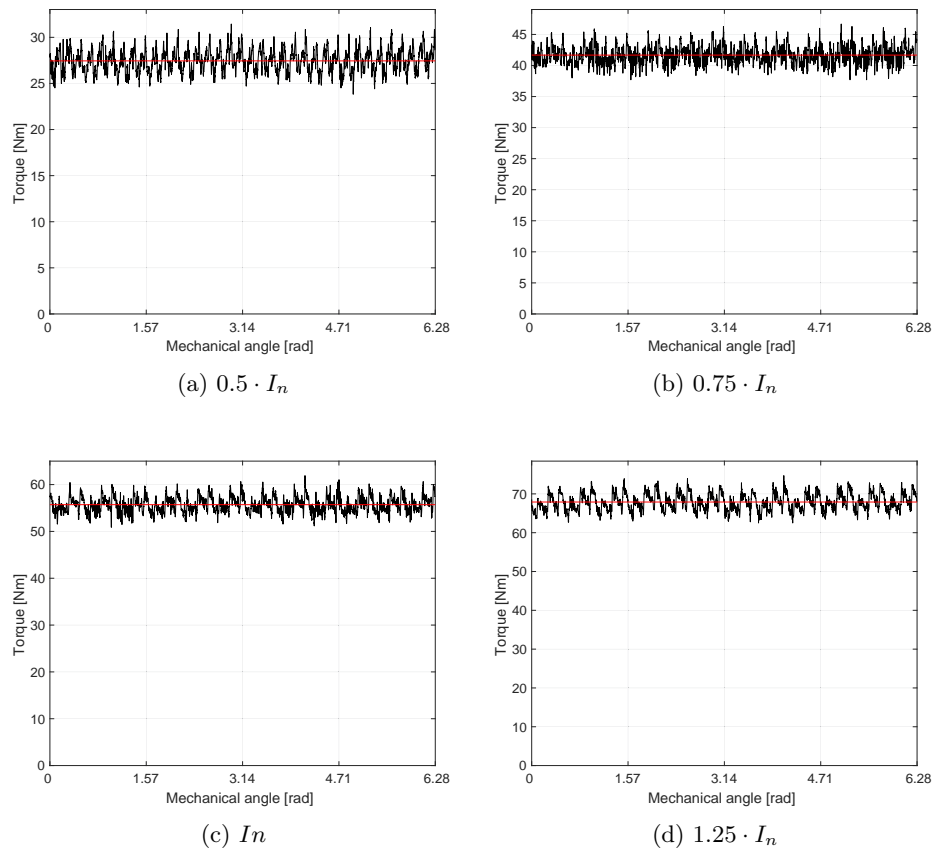


Figure 3.10: Torque in MTPA condition

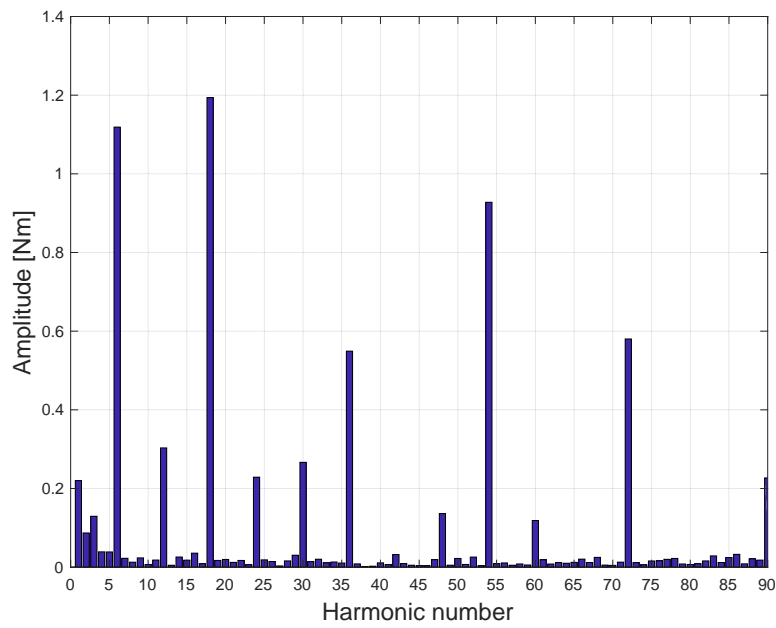


Figure 3.11: Harmonic content of torque operating in MTPA condition and at nominal current

### 3.3 Test bench for fast speeds

The fast bench used for the measurements is composed of:

- Master motor: induction three-phase motor having a nominal power of 5.5 [kW].
- Master inverter.
- Slave motor: IPM-FI.
- Slave inverter.
- Steel structure.
- Mechanical seals.
- dSPACE DS1104.
- Computer.
- Cooling fan.
- Variable AC power supply for the slave inverter.
- DC power supply.
- Torque meter: 100 [Nm].
- Amplifier and filter for the signals of the torque meter.
- RC filter for voltage measurements.
- Voltage differential probes.



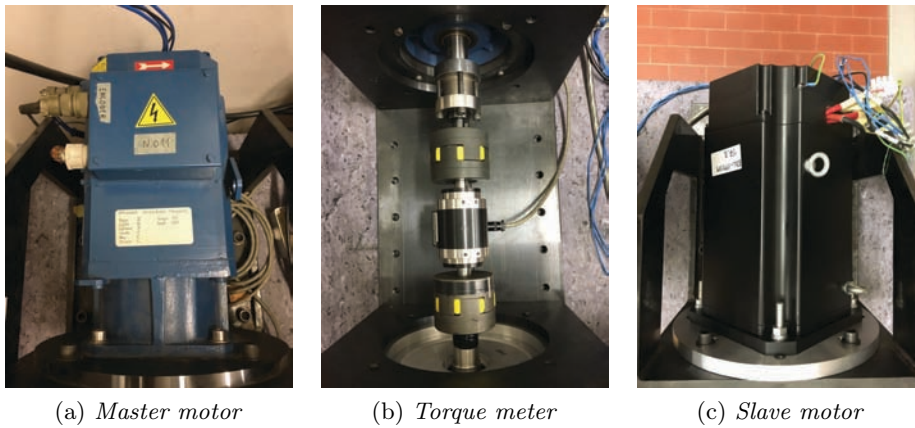


Figure 3.12: Main elements of the fast bench

The figure 3.12 represents the main elements of the fast bench. As in the case of the slow bench the motors must be fixed in the desired position according to the required distance from each other. Before every test the supports must be anchored to structure using screws. The connection between master and slave motor, rotating around the same axis, includes mechanical seals and a torque meter. The torque meter is connected to a filter and to an amplifier which provides a signal in the range  $0 - 5$  [V]. The signal is acquired and elaborated by the dSPACE board. In this case only one torquemeter, that has  $100$  [Nm] as full-scale has been used. The master motor is an induction motor and has the following parameters:

- Nominal power:  $P_n = 5.5$ [kW].
- Nominal speed:  $n_n = 2250$ [rpm].
- Nominal torque:  $T_{max} = 23$ [Nm].
- Maximum torque:  $T_n = 48$ [Nm].
- Nominal rms voltage:  $V_n = 295$ [V].
- Nominal rms current:  $I_n = 17$ [A].

The master has an encoder which transmits the position signal to the inverter. It regenerates the signal and makes it available to an output as a signal similar to that received from an incremental encoder ( $1024$  [pulses/rpm]). Considering the rigid connection among the motors, the position obtained is valid for both motors. The user manually sets the start of the rotation and the speed of the master motor using an interface which acts on the master inverter. The speed is shown on a four cyphers display. The master inverter is connected to a brake chopper in order to dissipate the energy produced by

the master motor during the tests. The slave inverter is fed by a variable AC power supply, which is fed by a DC power supply. The phase-to-phase voltage is not directly measurable, because there is the hysteresis of the inverter and this effect overlaps to the waveforms. This effect can be canceled using an RC low-pass filter, in fact the hysteresis effect is in a really high frequency range. To collect the measures of phase-to-phase voltage, two differential probes are connected to three points of the filter, which links resistances and capacitors. The filter introduces a gain and a phase shift which are linked to the electric angular velocity. It is important bear in mind these effects to achieve good results from the measures. The gain is evaluated with 3.2 and the phase shift with 3.3.

$$G(\Omega_{me}) = \frac{1}{1 + (R_f \cdot C_f \cdot \Omega_{me})^2} \quad (3.2)$$

$$(\Omega_{me}) = \arctan(R_f \cdot C_f \cdot \Omega_{me}) \quad (3.3)$$

The slave inverter controls signals from the real time dSPACE DS1104 board. It provides references and collects data. MATLAB and ControlDesk communicate. MATLAB scripts are used to define variables, to execute calculation, to save files. ControlDesk scripts create the real references for the inverter and define which gate is an input and which is an output.

### 3.3.1 Software

The system is controlled using MATLAB and ControlDesk. MATLAB scripts assign values of the variables, collect data and are used for the post elaboration. ControlDesk scripts work at a lower level to generate the references for the inverters and collect position data from the encoder. This last category of programs operate cyclically. ControlDesk contains offsets due to the slave inverter. The user sets in MATLAB scripts the speed, the polar pair number, the full-scale of the torque meter and the range and steps of currents. The measure is not done at nominal speed but for a value of speed, which allows to observe the back electric motrice forces without confusing them with the noise. In this case we have operated with a speed equal to 200 [rpm]. In the first part of the test it is necessary to follow procedures in order to identify the positions of the d and q axes. Using the first procedure the motor is fed with a DC current and the user manually rotates the rotor until it reaches one of the equilibrium positions, where it becomes difficult to move the shaft further. After that the DC supply is removed. After this procedure MATLAB provides commands in order to realize an automatic identification of the axes measuring the electromotive forces due to the rotation forced by the master. The plug, which brings energy to the inverter, is disconnected to

be sure that the slave motor does not receive any currents and the user sets the speed for the master motor. Typing "start" on the command window the procedure starts. The system acquires phase-to-phase voltage samples and the information coming from the encoder taking into account the phase shift due to the filter. The MATLAB script identifies the essential angle in order to guarantee the correct correspondence between the  $d$  and the  $q$  motor axes and the  $d$  and the  $q$  feeding currents, using the available data. After this part the plug which feeds the slave inverter is reconnected and the system is ready to start the test. Using cycles to vary the currents step by step MATLAB realizes matrixes for  $\Lambda_d$ ,  $\Lambda_q$ ,  $V_d$ ,  $V_q$  and the torque. The data is saved and subsequently used to show the results graphically.

### 3.3.2 Mapping of flux and torque

A map of the flux and of the torque is the aim of this test. There is a first part in which it is important to identify the  $d$  axis of the motor in order to have a correspondence between that axis and the  $d$  axis defined in the MATLAB script. In order to extrapolate the information relative to the fluxes a method has been used that permits the knowledge of the resistance to be avoided. This method consists of two tests, the first at  $(I_d, I_q)$  and the second at  $(I_d, -I_q)$ . For this method, working in a  $d$ - $q$  synchronous system is necessary. Therefore starting from the knowledge of the phase-to-phase voltages, that have been measured, the following steps allow to define the desired system of equation. The relation 3.4 allows to get information of the phase-to-phase voltage from the probes.

$$V_{ab} + V_{bc} + V_{ca} = 0 \quad (3.4)$$

As a first point the passage from phase-to-phase voltages to phase-voltages is required.

$$\begin{aligned} V_{ab} &= V'_a - V'_b \\ V_{bc} &= V'_b - V'_c \end{aligned} \quad (3.5)$$

Imposing  $V'_b = 0$ .

$$\begin{aligned} V'_a &= V_{ab} \\ V'_b &= 0 \\ V'_c &= -V_{bc} \end{aligned} \quad (3.6)$$

A homopolar component can be present.

$$V_0 = \frac{V'_a + V'_b + V'_c}{3} \quad (3.7)$$

The system can be rewritten.

$$\begin{aligned} V_a &= V'_a + V_0 \\ V_b &= V'_b + V_0 \\ V_c &= V'_c + V_0 \end{aligned} \quad (3.8)$$

The next step is to transform the equations from a  $a, b, c$  system to an  $\alpha,$  system.

$$\begin{aligned} V_\alpha &= \frac{2 \cdot V_a - V_b - V_c}{3} \\ V_\beta &= \frac{V_b - V_c}{\sqrt{3}} \end{aligned} \quad (3.9)$$

In conclusion the equations are transformed from a  $\alpha,$  system to a  $d, q$  system.

$$\begin{aligned} V_d &= V_\alpha \cdot \cos \theta_{dq} + V_\beta \cdot \sin \theta_{dq} \\ V_q &= -V_\alpha \cdot \sin \theta_{dq} + V_\beta \cdot \cos \theta_{dq} \end{aligned} \quad (3.10)$$

It can also be written in a another way.

$$V_{dq} = V_d + j \cdot V_q \quad (3.11)$$

In order to obtain correct results it is crucial to get a correct angle  $\theta_{dq}$ .

$$\theta_{dq} = p \cdot \theta_m + \theta_{\text{theta\_delta}} - \theta_{\text{delta\_ang}} \quad (3.12)$$

Equation 3.12 contains:

- $\theta_m$  is the angle read by the encoder.
- $\theta_{\text{theta\_delta}}$  is the angle in order to have the coincidence between the  $d$  and  $q$  axes of motor and of the currents.
- $\theta_{\text{delta\_ang}}$  includes any possible phase shift due to filters.

Considering  $V_d$  and  $V_q$  achieved as previously described, the following equations that are valid in a steady state can be used.

$$\begin{aligned} V_d &= R \cdot I_d - \Lambda_q(I_d, I_q) \cdot \Omega_{me} \\ V_q &= R \cdot I_q + \Lambda_d(I_d, I_q) \cdot \Omega_{me} \end{aligned} \quad (3.13)$$

Starting from the 3.13, for the couple  $(I_d, I_q)$ :

$$\begin{aligned} V_{d1} &= R \cdot I_d - \Lambda_q(I_d, I_q) \cdot \Omega_{me} \\ V_{q1} &= R \cdot I_q + \Lambda_d(I_d, I_q) \cdot \Omega_{me} \end{aligned} \quad (3.14)$$

and for the couple  $(I_d, -I_q)$ :

$$\begin{aligned} V_{d2} &= R \cdot I_d - \Lambda_q(I_d, -I_q) \cdot \Omega_{me} \\ V_{q2} &= -R \cdot I_q + \Lambda_d(I_d, -I_q) \cdot \Omega_{me} \end{aligned} \quad (3.15)$$

If the two tests are carried out in a relatively short temporal range, the resistance value can be considered unvaried. The two systems can be handled as shown in the following steps.

$$\begin{aligned} V_{d1} - V_{d2} &= \Lambda_q(I_d, -I_q) \cdot \Omega_{me} - \Lambda_q(I_d, I_q) \cdot \Omega_{me} \\ V_{q1} + V_{q2} &= \Lambda_d(I_d, -I_q) \cdot \Omega_{me} + \Lambda_d(I_d, I_q) \cdot \Omega_{me} \end{aligned} \quad (3.16)$$

Observing the figures 3.15 and 3.16 a symmetry property can be observed. Therefore the following relations can be written.

$$\begin{aligned} \Lambda_d(I_d, I_q) &= \Lambda_d(I_d, -I_q) \\ \Lambda_q(I_d, I_q) &= -\Lambda_q(I_d, -I_q) \end{aligned} \quad (3.17)$$

Using 3.17 the system 3.16 can be modified.

$$\begin{aligned} V_{d1} - V_{d2} &= -2 \cdot \Lambda_q(I_d, I_q) \cdot \Omega_{me} \\ V_{q1} + V_{q2} &= 2 \cdot \Lambda_d(I_d, I_q) \cdot \Omega_{me} \end{aligned} \quad (3.18)$$

In conclusion the fluxes are:

$$\begin{aligned} \Lambda_d(I_d, I_q) &= \frac{V_{q1} + V_{q2}}{2 \cdot \Omega_{me}} \\ \Lambda_q(I_d, I_q) &= -\frac{V_{d1} - V_{d2}}{2 \cdot \Omega_{me}} \end{aligned} \quad (3.19)$$

In this way potential offsets are canceled and knowledge of the resistance is not necessary.

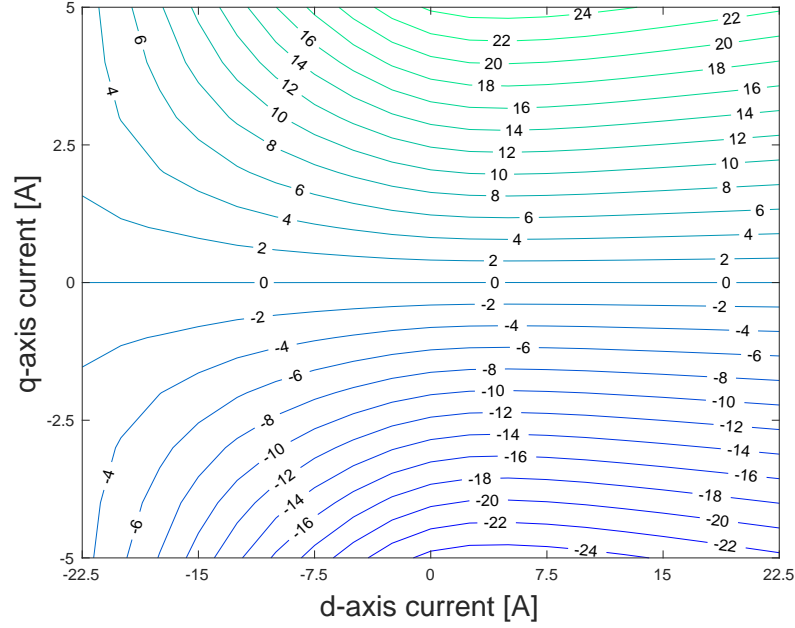


Figure 3.13: Measured torque map at fast bench

### 3.3.3 Results

As a first point it is important to compare the results obtained by the torque meter and the torque evaluated as shown in 3.20.

$$T = \frac{3}{2} \cdot p \cdot (\Lambda_d(I_d, I_q) \cdot I_q - \Lambda_q(I_d, I_q) \cdot I_d) \quad (3.20)$$

Figure 3.13 shows the torque map obtained by the torque meter and in 3.14 the comparison of the two torque trends can be appreciated. This map is obtained varying  $I_d$  from  $-22.5[\text{A}]$  to  $22.5[\text{A}]$  with a step variation of  $2.5[\text{A}]$  and  $I_q$  from  $-5[\text{A}]$  to  $5[\text{A}]$  with a step variation of  $1[\text{A}]$  at a speed of  $220[\text{rpm}]$ . The trends are similar, there are no offsets and the symmetry along the  $d$  axis can be observed.

Using the method previously described, the fluxes and the cross coupling effect can be observed in the figures 3.15 and 3.16. In order to get a better comprehension of the phenomena, the graph 3.17 can be taken into account. In conclusion the flux map can be shown in figure 3.18 considering the flux as expressed in the following equation:

$$\Lambda = \sqrt{\Lambda_d^2 + \Lambda_q^2} \quad (3.21)$$

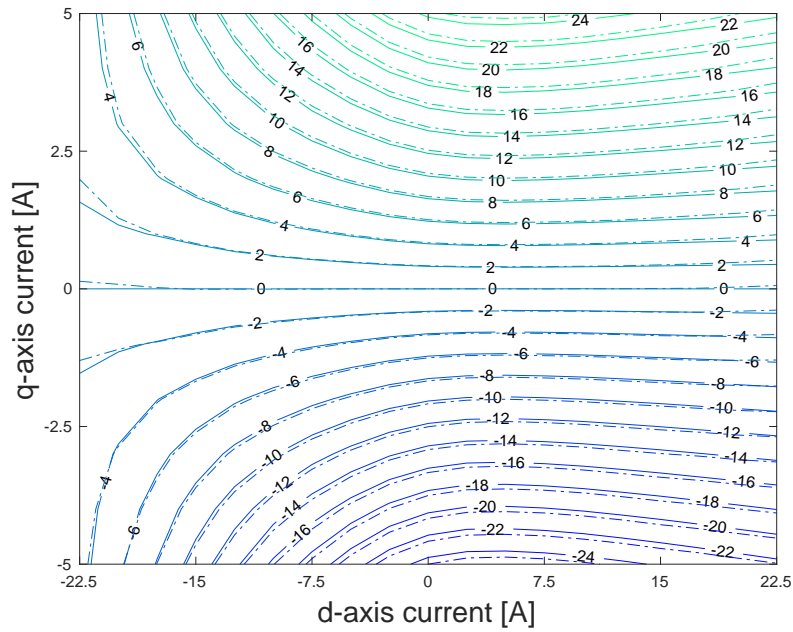


Figure 3.14: Calculated (dashed lines) and measured torque map at fast bench

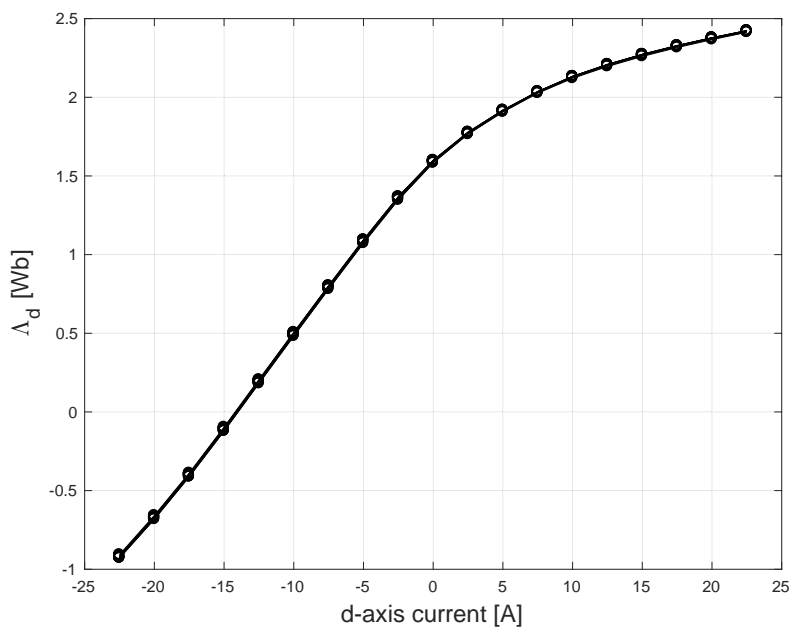


Figure 3.15: d-axis flux

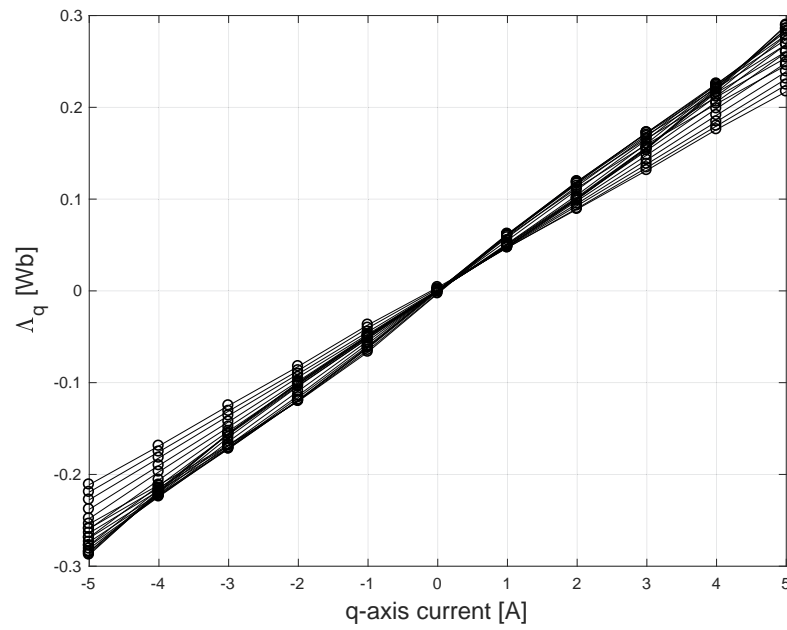
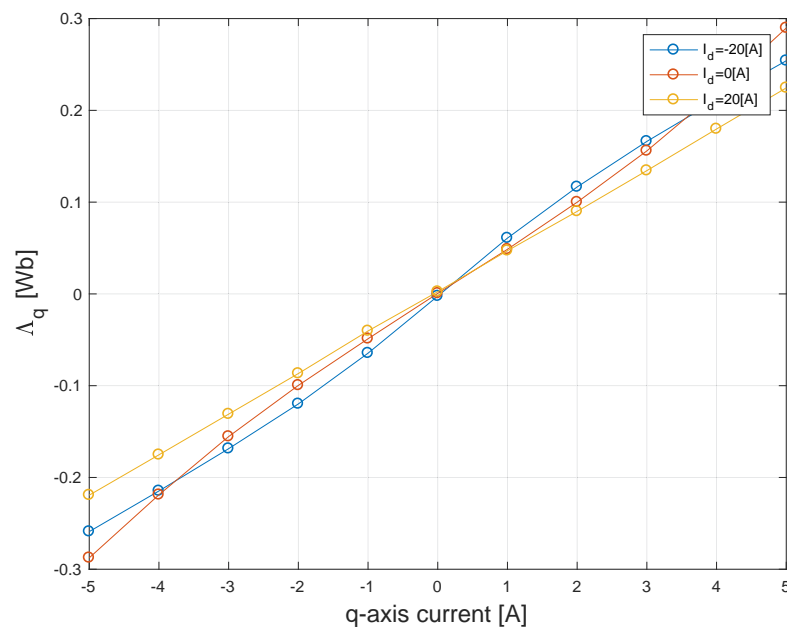


Figure 3.16: q-axis flux

Figure 3.17: q-axis flux, at  $I_d = -20$  [A],  $I_d = 0$  [A],  $I_d = 20$  [A],



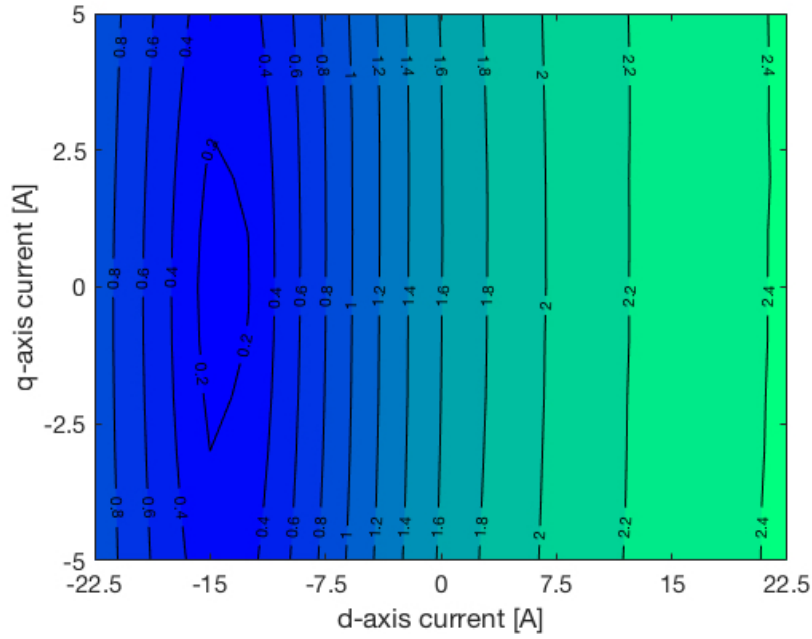


Figure 3.18: Flux map

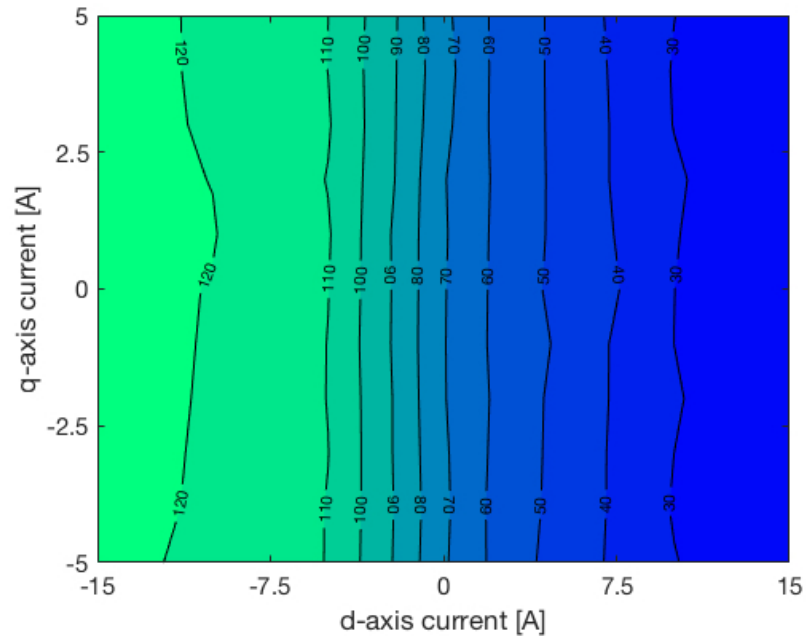
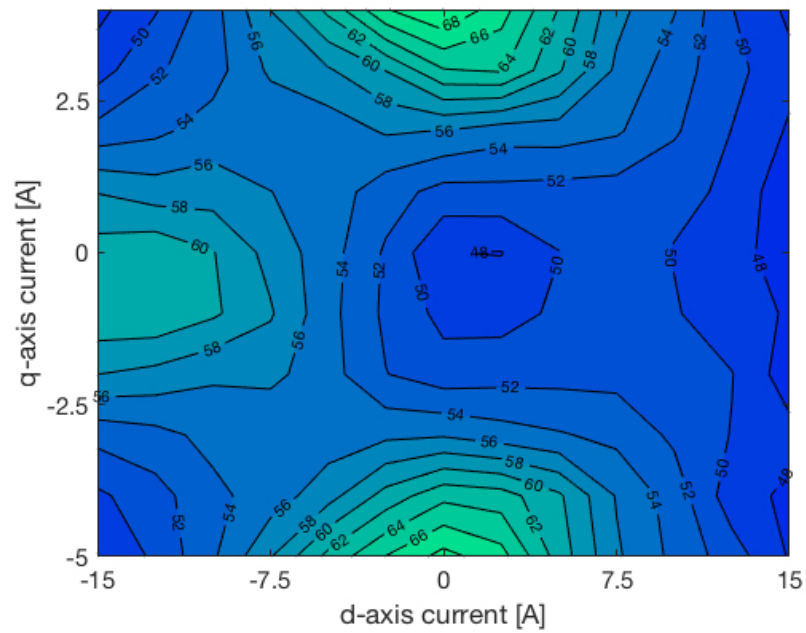
With the collected data it is possible to create a map of  $L_d$  and  $L_q$ , shown in figures 3.19 and 3.20. This is done using the following equations:

$$L_d = \frac{\Lambda'_d - \Lambda''_d}{I'_d - I''_d} \Big|_{I_q = \text{const}} \quad (3.22)$$

$$L_q = \frac{\Lambda'_q - \Lambda''_q}{I'_q - I''_q} \Big|_{I_d = \text{const}} \quad (3.23)$$

Furthermore using the definition of saliency ratio which is the ratio between  $L_d$  and  $L_q$  as expressed in the equation 3.24, a saliency ratio map has been plotted in figure 3.21.

$$= \frac{L_d}{L_q} \quad (3.24)$$

Figure 3.19:  $L_d$  mapFigure 3.20:  $L_q$  map

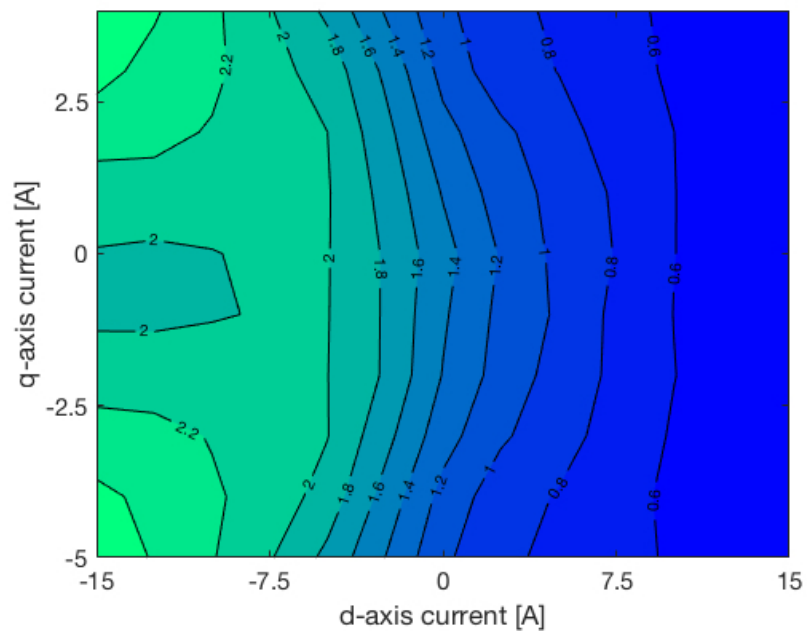


Figure 3.21: Saliency ratio map

### 3.4 Back emf

For the last measurement an oscilloscope has been used to show the back emf. In figure 3.22, the trends can be appreciated. Using MATLAB, the trends have been reproduced and the harmonic content evaluated as show in 3.23 and 3.24. Observing the results and the motor data sheet it can be noted that the measurements have been done correctly. The nominal rms phase voltage on data sheet is 202.2[V] that is a rms phase-to-phase nominal voltage of 350.2 [V] and the rms value from the oscilloscope taking into account the gain of the probes is 342[V].

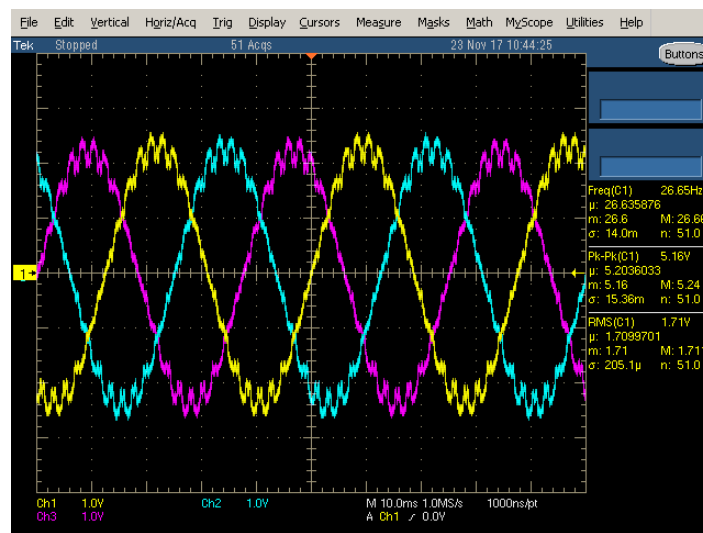


Figure 3.22: Back emf seen on oscilloscope

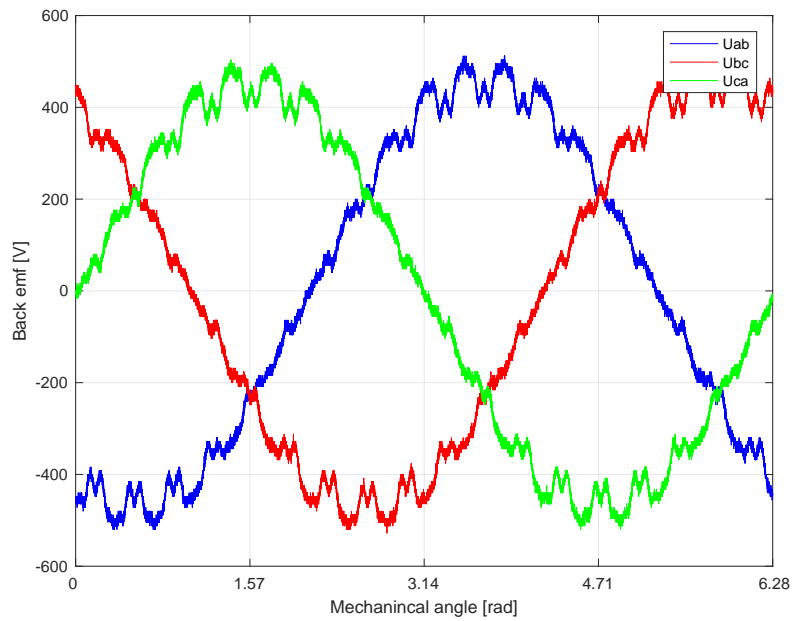


Figure 3.23: Back emf

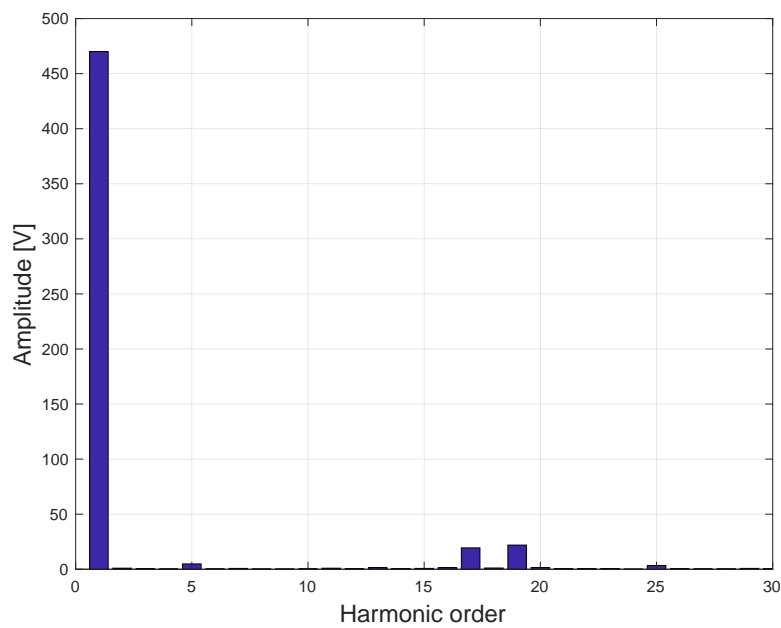


Figure 3.24: Harmonic content back emf

## Chapter 4

# Electric drive

In this section a suitable electric drive for the FI-IPM motor is presented. The target is an optimal control of the torque applying a plug-and-play method.

### 4.1 Motor model

First of all it is necessary to identify the fundamental equations that describe the behavior of the motor. In a  $dq$  rotating reference frame, the stator voltage equations are:

$$\begin{aligned}u_d &= R \cdot I_d + \frac{d\lambda_d}{dt} - \omega_{me} \cdot \lambda_q \\u_q &= R \cdot I_q + \frac{d\lambda_q}{dt} + \omega_{me} \cdot \lambda_d\end{aligned}\tag{4.1}$$

In the equations the subscripts  $d$  and  $q$  refer to the d-axis and the q-axis values of current, voltage and flux.  $R$  is the stator resistance and  $\omega_{me}$  is the electrical angular speed.

The magnitude of the stator current can be written as:

$$i_s = \sqrt{i_d^2 + i_q^2}\tag{4.2}$$

The current components along the  $d$  axis and the  $q$  axis are nonlinear functions of the flux components:

$$\begin{aligned}i_d &= i_d(\lambda_d, \lambda_q) \\i_q &= i_q(\lambda_d, \lambda_q)\end{aligned}\tag{4.3}$$

A nonlinear inductor should neither generate nor dissipate energy. The reciprocity theorem is valid and considering the works [16] and [17] the following relation can be written as:

$$\frac{i_d}{\lambda_q} = \frac{i_q}{\lambda_d} \quad (4.4)$$

At the end the equation to evaluate the torque is:

$$T = \frac{3 \cdot p}{2} \cdot (\lambda_d \cdot i_q - \lambda_q \cdot i_d) \quad (4.5)$$

## 4.2 Algebraic magnetic model and fitting

The data can be collected by either measures or fem analysis. However the problem is, that this collection of data looks like a cloud of points. It is really much more complex to reverse engineer a model from data than it is to reverse engineer a law. For a law, each data point falls on the function that describes the law but for a model, each data point falls around the function that describes the model. Having enough points, it may be possible to notice the structure of these distributions, and therefore make a good guess about the form of the model. Linear models are among the most used modeling methods. This kind of model uses a linear function to map a set of values to a set of normal distributions. For linear models also including the generalized linear models with exponential distributions, the best model will be the one that has the smallest residual sum of squares. A residual is the distance between the mean of the predicted distribution and the data point observed. These residuals can be either positive or negative. The magnitude of a residual can be calculated evaluating the square of the residual. Therefore the least squares model will be the model that presents the smallest squared residuals. In fact it means that the model can be used to recreate a trend close to the data points. An algebraic magnetic model is presented in [18] and [19]. In the mentioned works this model simplifies the self-commissioning. The required parameters are extracted by fitting the model using the data of the tests. Neglecting the presence of the cross-saturation, for the moment, a polynomial function can be used for modeling the currents:

$$i_d(\lambda_d) = (a_{d0} + a_{d1} \cdot |\lambda_d| + \dots + a_{dn} \cdot |\lambda_d|^n) \cdot \lambda_d - i_f \quad (4.6)$$

$$i_q(\lambda_q) = (a_{q0} + a_{q1} \cdot |\lambda_q| + \dots + a_{qn} \cdot |\lambda_q|^m) \cdot \lambda_q \quad (4.7)$$

Where  $a_{d0} \dots a_{dn}$ ,  $a_{q0} \dots a_{qn}$  are coefficients and  $n$ ,  $m$  are the highest exponents. The component  $i_f$  is due to the presence of the magnets. As been specified in the reference, usually  $n = 4 \dots 7$  and  $m = 1$  offer a good fitting. However an iterative procedure can be implemented to evaluate the results of the fitting varying the choice of the exponents.

### 4.2.1 Fitting using a polynomial function

Neglecting for the moment the presence of the cross-saturation, a polynomial function can be used for modeling the currents:

$$i_d(\lambda_d) = (a_{d0} + a_{d1} \cdot |\lambda_d| + \dots + a_{dn} \cdot |\lambda_d|^n) \cdot \lambda_d - i_f \quad (4.8)$$

$$i_q(\lambda_q) = (a_{q0} + a_{q1} \cdot |\lambda_q| + \dots + a_{qn} \cdot |\lambda_q|^m) \cdot \lambda_q \quad (4.9)$$

Where  $a_{d0} \dots a_{dn}$ ,  $a_{q0} \dots a_{qn}$  are coefficients and  $n$ ,  $m$  the highest exponents. The component  $i_f$  is due to the presence of the magnets. Fixing the exponents as shown in the table, the coefficients can be obtained with the linear least square method.

$S$	$T$	$U$	$V$
7	0	6	0

Table 4.1: Exponential coefficients of the algebraic model

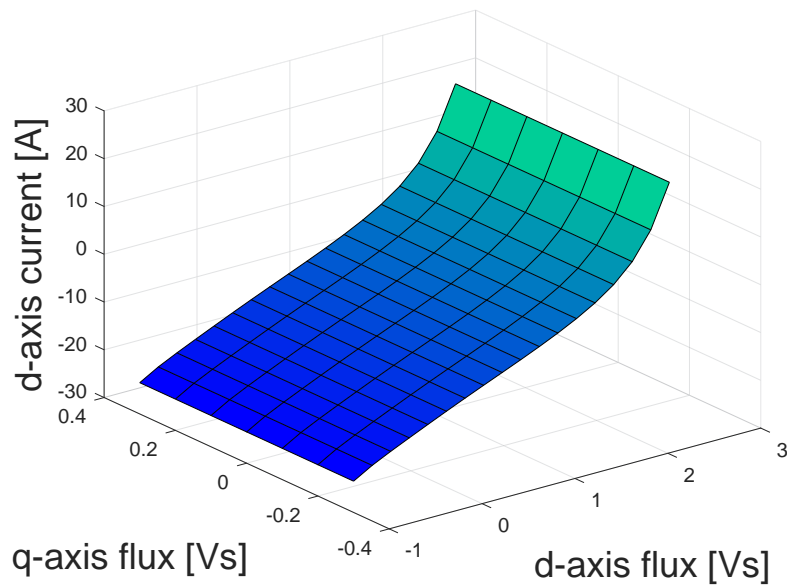
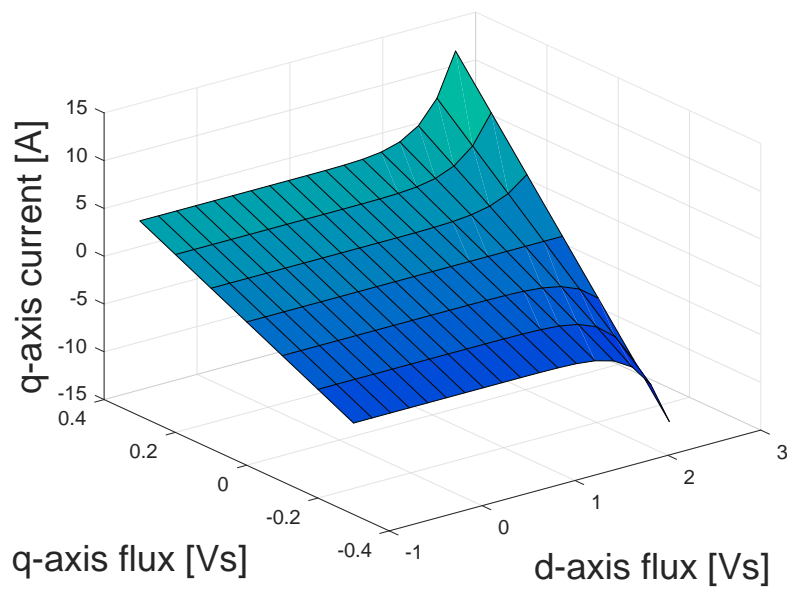
The figures 4.1 and 4.2 have been obtained. A two-dimensional view gives a clearer idea of the fitting 4.3 and 4.4. The fitting still remains good, if some exponential parameters are neglected. In fact a second simplified system of equation can be considered:

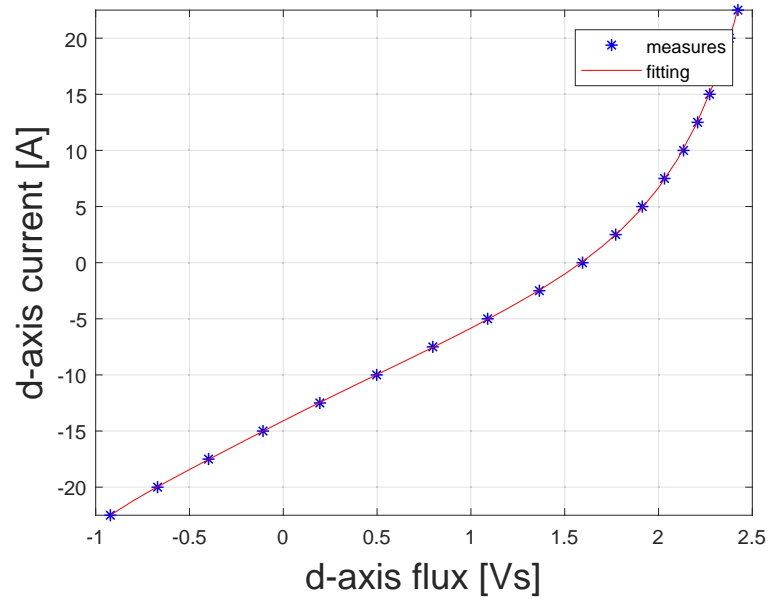
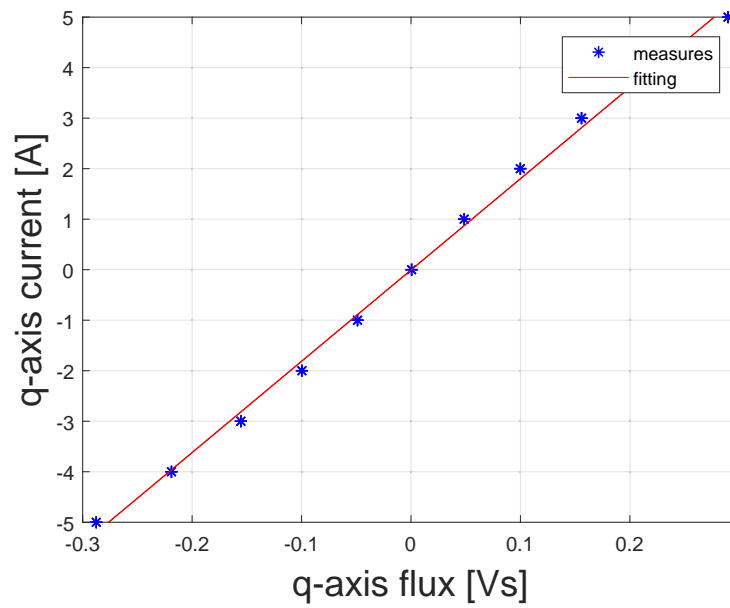
$$\begin{aligned} i_d(\lambda_d) &= (a_{d0} + a_{dd} \cdot |\lambda_d|^S) \cdot \lambda_d - i_f \\ i_q(\lambda_q) &= (a_{q0} + a_{qq} \cdot |\lambda_q|^T) \cdot \lambda_q \end{aligned} \quad (4.10)$$

Where  $a_{d0}, a_{q0}$  can be defined as the inverse unsaturated inductance along the  $d$  axis and  $q$  axis respectively. The parameters  $S$  and  $T$  define the shape of the saturation characteristics. The coefficients, except for  $i_f$ , of the polynomial function must be positive or equal to 0 in order to avoid non-monotonic function outside the range.

The result of the fitting is still good as can be appreciated in 4.5 and 4.6.



Figure 4.1: Three-dimensional fitting with a polynomial function,  $d$  axisFigure 4.2: Three-dimensional fitting with a polynomial function,  $q$  axis

Figure 4.3: Two-dimensional fitting with a polynomial function,  $d$  axisFigure 4.4: Two-dimensional fitting with a polynomial function,  $q$  axis

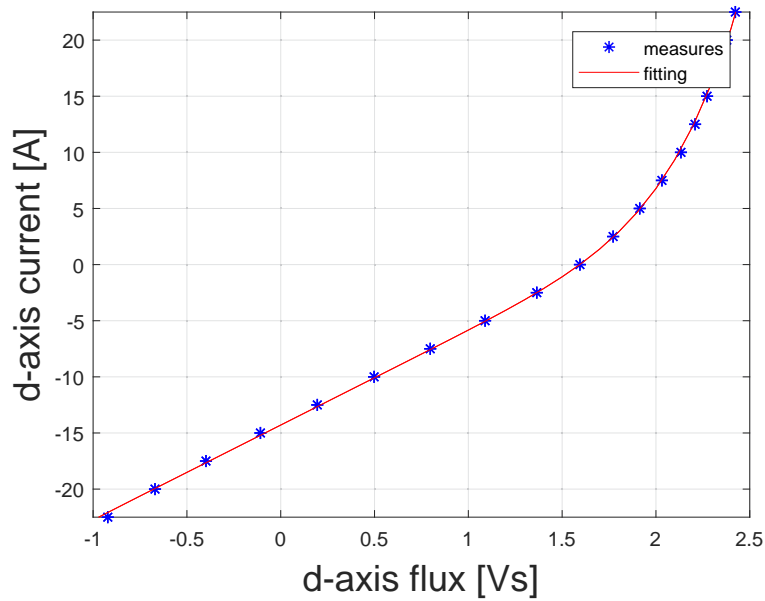


Figure 4.5: Two-dimensional fitting with a polynomial function omitting part of the coefficients,  $d$  axis

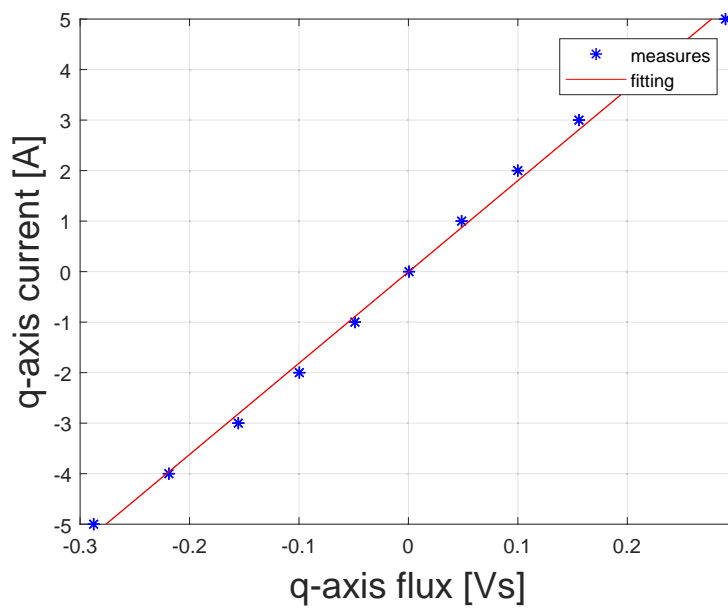


Figure 4.6: Two-dimensional fitting with a polynomial function omitting part of the coefficients,  $q$  axis

The differences between the two fitting models are quite small if d-axis is considered. The same can not be said about the q-axis where the characteristic assumes a linear shape. Anyway the simplified version has been selected to reduce the complexity of the system.

#### 4.2.2 Aalto fitting tool

At Aalto University a script to get an optimal fitting is available and it has been applied. As described in the mentioned publications the model can be slightly modified in order to include the cross-saturation effect. Considering the reciprocity condition 4.4 a new system of equations can be written:

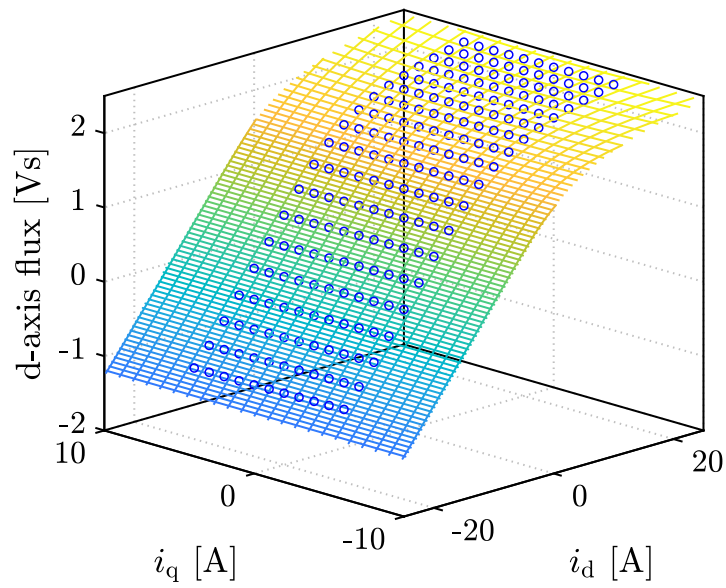
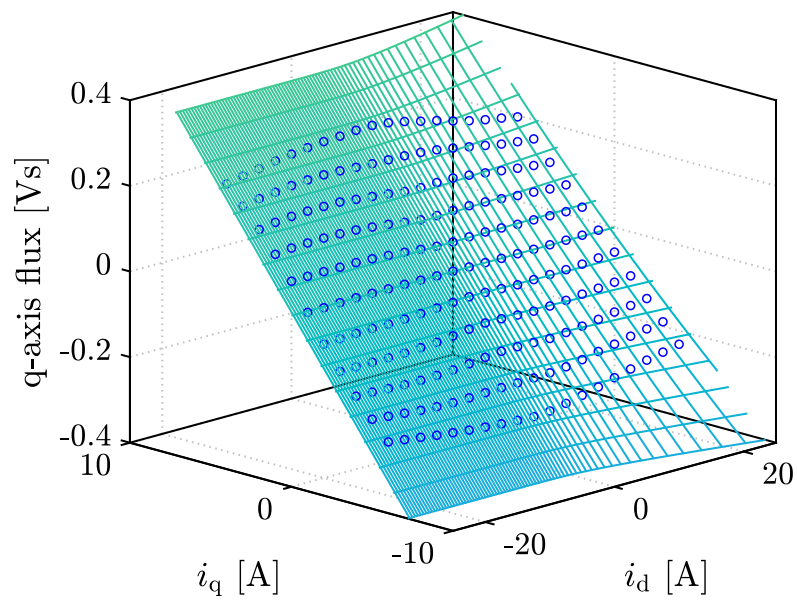
$$\begin{aligned} id(\lambda_d, \lambda_q) &= (a_{d0} + a_{dd} \cdot |\lambda_d|^S + \frac{a_{dq}}{V+2} \cdot |\lambda_d|^U \cdot |\lambda_q|^{V+2}) \cdot \lambda_d - i_f \\ iq(\lambda_d, \lambda_q) &= (a_{q0} + a_{qq} \cdot |\lambda_q|^T + \frac{a_{dq}}{U+2} \cdot |\lambda_d|^{U+2} \cdot |\lambda_q|^V) \cdot \lambda_q \end{aligned} \quad (4.11)$$

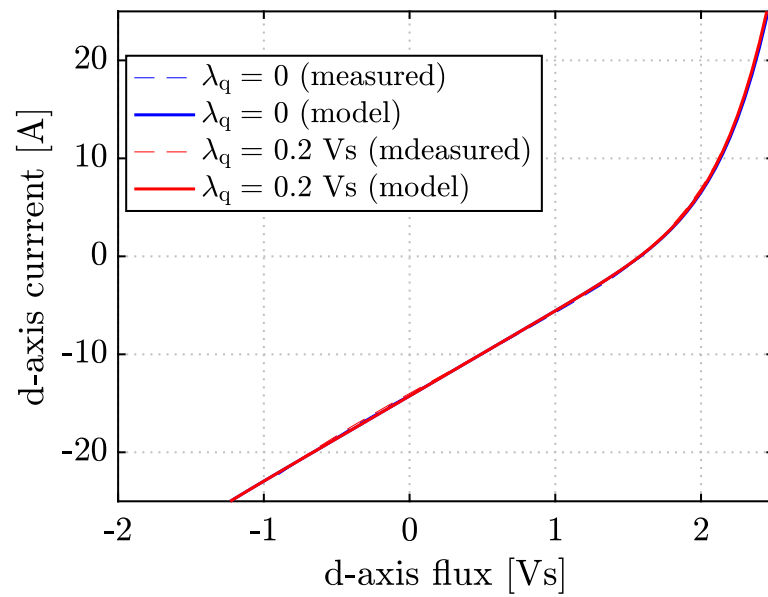
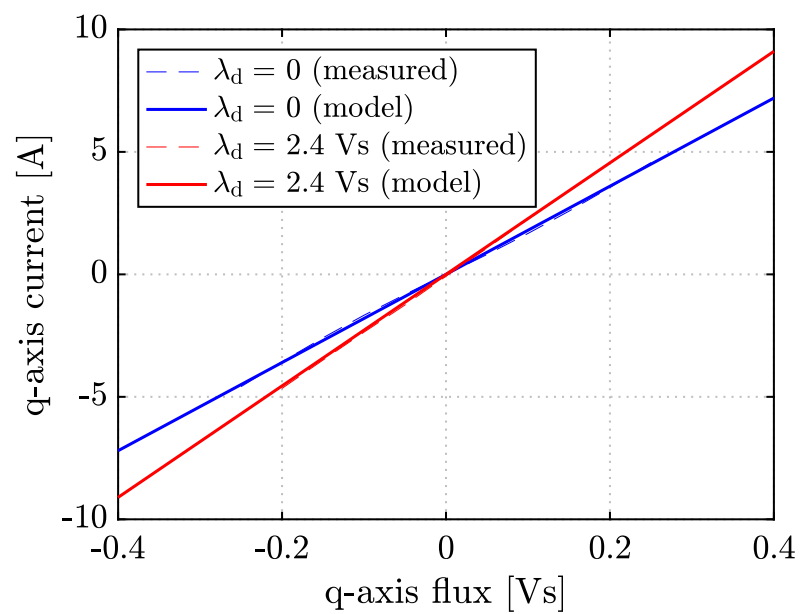
Using the previously set exponential coefficients, the optimal parameters have been found and reported here:

$a_{d0}$	$a_{dd}$	$a_{q0}$	$a_{qq}$	$a_{dq}$	$i_f$
08,677	0,013	17,997	0,000	0,035	14,251

Table 4.2: Fitting parameters using Aalto's tool

Two three-dimensional and two two-dimensional maps show the resulting fitting. The following maps are obtained taking into account the collected data.

Figure 4.7: Three-dimensional fitting with Aalto's tool,  $d$  axisFigure 4.8: Three-dimensional fitting with Aalto's tool,  $q$  axis

Figure 4.9: Two-dimensional fitting with Aalto's tool,  $d$  axisFigure 4.10: Two-dimensional fitting with Aalto's tool,  $q$  axis

### 4.3 MTPA and MTPV locus

An important part of the work are the reference calculations. The implemented scheme is reported in figure 4.11. In order to apply it, the lookup tables of MTPA and of MTPV are required.

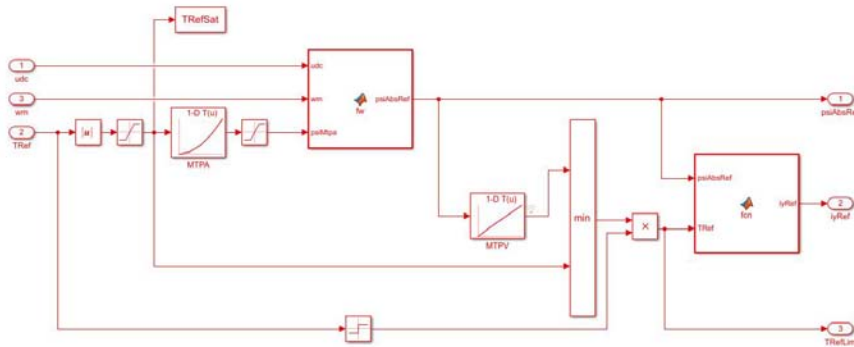


Figure 4.11: Reference calculations scheme

The optimal flux for the MTPA condition is obtained from a lookup table where the torque reference is the input. The MTPA flux  $\Lambda_{MTPA}$  is limited by the maximum available voltage leading to the optimal flux magnitude under voltage limit. The maximum voltage is strictly related to the voltage of the DC bus, consequently a variation in  $u_{DC}$  has effects on the references. The torque reference is the minimum among the values that are read by the lookup tables as can be seen in 4.11. The main advantages of this scheme is that optimal values of the torque and of the flux can be always obtained without any delays regardless of the input torque and speed. The required lookup tables can be calculated considering the circle diagram that has been evaluated. On it the MTPA, the MTPV, the current and voltage limits are shown. The matlab script is based on the following formulas that describe the behavior of the motor in steady state. The torque:

$$T = \frac{3 \cdot p}{2} \cdot [\Lambda_{PM} + (L_d - L_q) \cdot i_d] \cdot i_q \quad (4.12)$$

The maximum current:

$$i_s = \sqrt{i_d^2 + i_q^2} \leq i_{max} \quad (4.13)$$

The maximum flux linkage:

$$\lambda_s = \sqrt{(\Lambda_{PM} + L_d \cdot id)^2 + (L_q \cdot iq)^2} \leq \frac{u_{max}}{|\omega_{me}|} \quad (4.14)$$

Imposing the derivative of the torque with respect to the current along the  $d$  axis to be equal to zero the definition of MTPA can be used to identify the locus. The MTPV locus has been evaluated in a similar way. The resultant circle diagram is shown in figure 4.12.

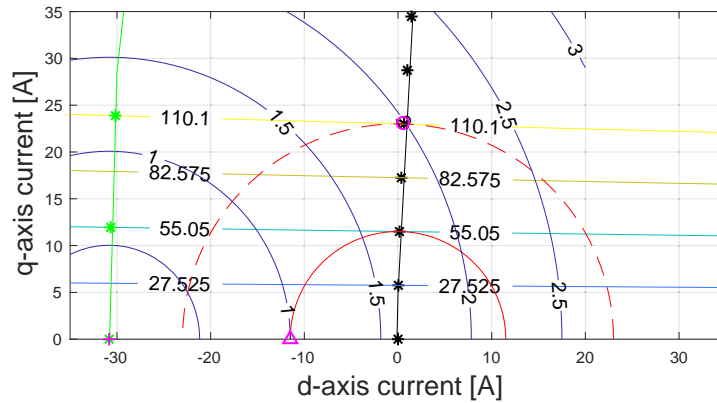


Figure 4.12: Circle diagram: MTPA locus (black), MTPV (green), voltage limit (blue) and the current limit (red)

The black color is for the MTPA: the stars represent the points and the line is the interpolation. The green is used for the MTPV: the stars represent the points and the line is the interpolation. The red line shows the nominal current limit, while the dashed red line shows the current limit of a current that is three times the nominal. The colored lines represent the torque. The blue is for the voltage limit. In addition some crucial points are marked in magenta. These are:

- the center of the ellipses of the voltage limit;



- the intersection between the abscissa and the current limit;
- the intersection between the MTPA and the current limit.

## 4.4 Lookup tables

The calculation for the optimal flux linkage or current references is usually done off-line. A lookup table replaces computation with a simpler indexing operation and consequently retrieving a value from the memory instead can save significant processing time. Having the data from the measures this approach is particularly suitable. In [20] a lookup table computation method was presented. The procedure is based on the Brent algorithm [21] and the Powell dogleg algorithm [22]. The developed script has been slightly modified by the authors of the paper to work with a motor, which has an inverse saliency. The lookup tables for this motor are based on the figures 4.13 and 4.14. Especially from the first image, the relation between torque and flux in MTPA, MTPV and current limit conditions can be understood. Furthermore in figure 4.15 the circle diagram has been reported. The trends confirm what has been pointed out in figure 3.6 and 4.12 in the previously chapters.

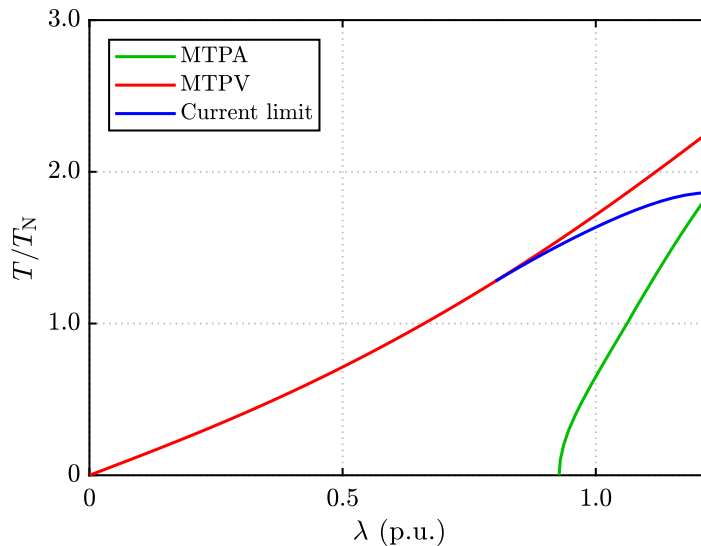


Figure 4.13: MTPA locus, MTPV and current limit

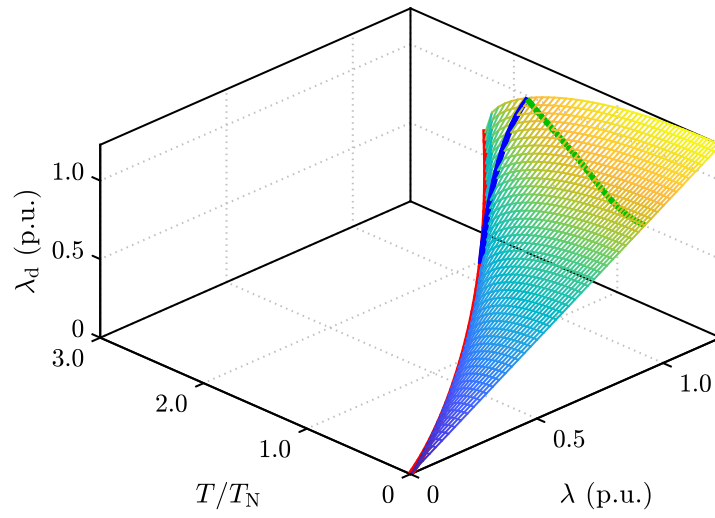
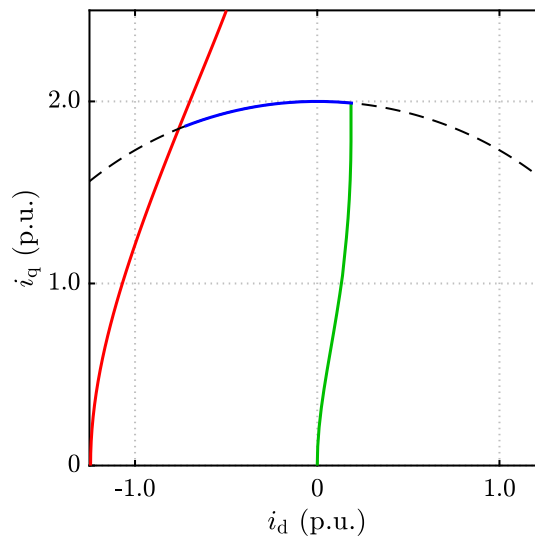


Figure 4.14: Feasible operating region

Figure 4.15: MTPA, MTPV and current limit in  $i_d$ ,  $i_q$  plane

## 4.5 Control system

A base Simulink sensorless model has been used to verify the correctness of the calculated lookup tables. The model has been modified in order to implement a stator-flux-oriented control. A digest about this control system has been produced by Aalto's team and it will be released by the end of the year. In it the variables under control are the magnitude of the stator flux and the component of the current that produces the torque. This simplifies the references calculation because only one-dimensional lookup tables of MTPA and MTPV must be implemented. The limitation of this system is due to the presence of some nonlinearities which appear in the inner control loop and this may disturb the correct performance of the system. Furthermore the dynamics are coupled and also this aspect can affect the performance. The paper offers a description of an exact input-output feedback linearization structure and of a state feedback controller with integral action and reference feedforward.

## 4.6 Simulations

The Simulink model has been used testing how the system react to a step of speed and the resulting plots are here reported. As can be observed in figure 4.16, the torque follows almost immediately the reference. In figure 4.17, the speed has been plotted and it reaches the desired value in 0.7 [s]. The variables under control and their references are reported in figure 4.18. The flux follows perfectly the reference while the current slightly differs from the reference in the first moments. The error in the position estimation can be noticed in figure 4.19. The amplitude is small and it quickly decreases to a negligible value.

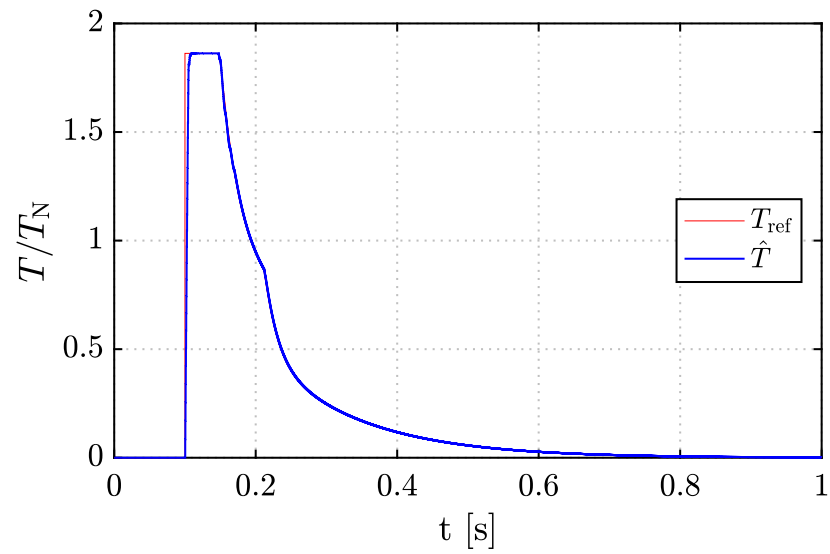


Figure 4.16: Trend of the torque

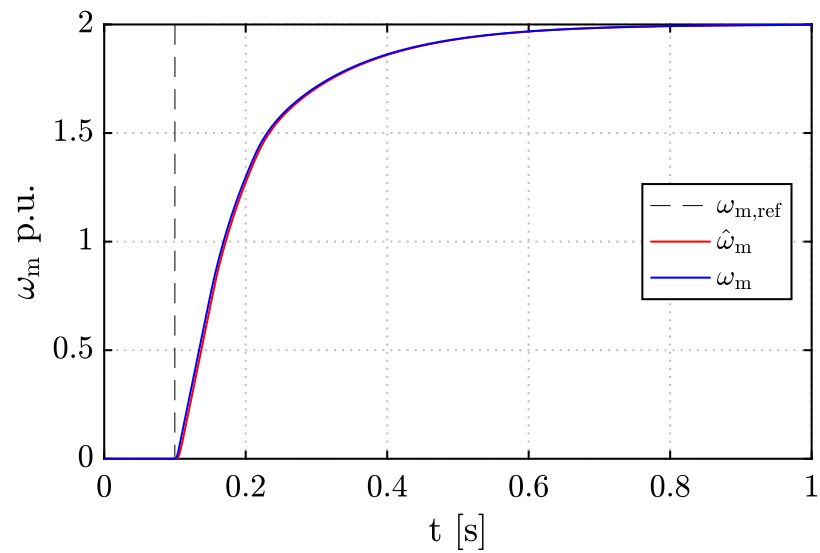


Figure 4.17: Trend of the speed

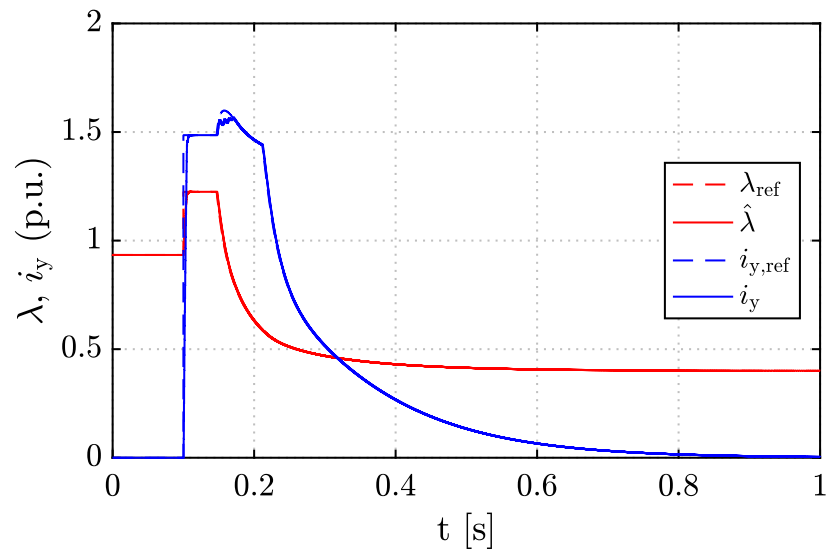


Figure 4.18: Trend of variables under control

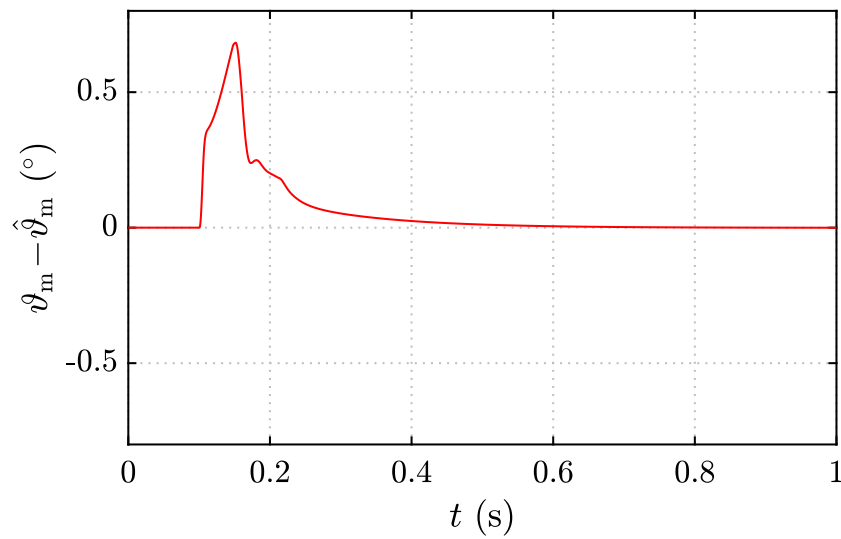


Figure 4.19: Position error

## Chapter 5

# Conclusions

In first part of the thesis, it has been pointed out how to obtain very accurate results from the measurements, taking into account the presence of cross-saturation. While doing measurements of the fluxes is convenient to evaluate the torque map because it gives the opportunity to verify the correctness of the fluxes. Furthermore it allows to carry out two different tests that take a lot of time if done individually. The measures at the bench for slow speeds provide the trends of the cogging torque and of the torque as function of the angle. The harmonics have been evaluated to point out the contribution of the magnets, due to the first harmonic, and the contribution of the reluctance torque proportional to the second harmonic. In addition, the cogging torque has been evaluated using two different torque-meters pointing out that a lower full-scale torque meter permits the achievement of more realistic results. The measurements of the torque as a function of  $\alpha_{ie}$  have had a crucial role to identify the MTPA. That also confirm the position of the MTPA that has been evaluated in the second part of the thesis when both MTPA and MTPV have been graphically represented. From the tests on the bench for high speeds instead, using the described method, the fluxes and the cross coupling effect have observed. The measurements have been used to obtain the mapping of torque and of the fluxes which characterize the motor. These trends have been compared with the FEM data confirming the correctness of the available data. In the second part of the thesis the focus has been on the reference calculations and particularly attention has been dedicated on the creation of the lookup tables. Several scripts have been realized to evaluate the effects of both the presence and the omission of the cross-saturation. In the chapter dedicated to the electric drive, it has been shown how to create an optimal fitting following the reference works. The difference between the collected data and the trend of the fitting functions is minimal and this testifies the good quality of the work. At the end the lookup tables have been implemented in the reference system of a Simulink sensorless model that has been suitably modified to apply a

## 5 Conclusions

---

stator-flux-oriented control. Considering the resulting figures which confirm the expected results, it is possible to affirm that the reference calculations have been evaluated correctly.





# Bibliography

- [1] N. Bianchi, "Performance analysis of an IPM motor with segmented rotor for flux-weakening application", in *Proc. 9th Int. Conf. Elect. Mach. Drives, Conf. Publ. 468*, pp. 49-53, 1999.
- [2] N. Bianchi, S. Bolognani, B. J. Chalmers, "Salient-rotor PM synchronous motors for an extended flux-weakening operation range", *IEEE Trans. Ind. Appl.*, vol. 36, no. 4, pp. 1118-1125, Jul./Aug. 2000.
- [3] B. J. Chalmers, L. Musaba, D. F. Gosden, "Synchronous machines with permanent magnet and reluctance rotor sections", *Proc. Int. Conf. Electrical machines*, pp. 185-189, 1994.
- [4] D. F. Gosden, B. J. Chalmers, L. Musaba, "Drive system design for an electric vehicle based on alternative motor types", *Proc. IEE Int. Conf. Power Electronics and Variable-Speed Drives*, pp. 710-715, 1994.
- [5] B. J. Chalmers, R. Akmese, L. Musaba, "Design and field-weakening performance of permanent-magnet/reluctance motor with two-part of rotor", *Proc. IEE*, pt. B, vol. 145, no. 2, pp. 133-139, 1998.
- [6] K. Akatsu, M. Arimitsu, S. Wakui, "Design and control of a field intensified interior permanent magnet synchronous machine", *IEEE Trans. Ind. Appl.*, vol. 126, no. 7, pp. 827-834, 2006.
- [7] S. Morimoto, Y. Takeda, T. Hirasu, K. Taniguchi, "Expansion of operating limits for permanent magnet motor by current vector control considering inverter capacity", *IEEE Trans. Ind. Appl.*, vol. 26, no. 5, pp. 866-871, Sep./Oct. 1990.
- [8] N. Limsuwan, Y. Shibukawa, D. D. Reigosa, "Novel design of flux-intensifying interior permanent magnet synchronous machine suitable for self-sensing control at very slow speed and power conversion", *IEEE Trans. Ind. Appl.*, vol. 47, no. 5, pp. 2004-2012, Sept./Oct. 2011.
- [9] P. Guglielmi, M. Pastorelli, A. Vagati, "Cross-saturation effect in IPM motors and related impact on zero-speed sensorless control", in *Conf. Rec. IEEE IAS Annu. Meeting*, pp. 2546-2552, 2005.

- 
- [10] P. Guglielmi, M. Pastorelli, A. Vagati, "Impact of cross-saturation effects in sensorless control of transverse-laminated synchronous reluctance motors", *IEEE Trans. Ind. Electron.*, vol. 53, no. 2, pp. 429-439, Apr. 2006.
- [11] P. Guglielmi, M. Pastorelli, A. Vagati, "Cross-saturation effects in IPM motors and related impact on sensorless control", *IEEE Trans. Ind. Appl.*, vol. 42, no. 6, pp. 1516-1522, Nov./Dec. 2006.
- [12] S. Wu, D. D. Reigosa, Y. Shibukawa, M. A. Leetmaa, R.D Lorenz, Y. Li, "Interior permanent magnet synchronous motor design for improving self-sensing performance at very slow-speed", in *Proc. ICEMS*, pp. 3278-3283, Oct. 2008.
- [13] D. Reigosa, K. Akatsu, N. Limsuwan, Y. Shikabuwa, R. D. Lorenz, "Self-sensing comparison of fractional slot pitch winding vs. distributed winding for FW- and FI-IPMSMs base on carrier signal injection at very slow speed", in *Proc. IEEE-ECCE*, pp. 3806-3813, Sep. 2009.
- [14] H. Kim, R. D. Lorenz, "Carrier signal injection based sensorless control methods for IPM synchronous machine drives", in *Conf. Rec. IEEE IAS Annu. Meeting*, pp. 977-984, 2004.
- [15] D. Raca, P. Garcia, D. Reigosa, F. Briz, R. D. Lorenz, "A comparative analysis of pulsating vs. rotating vector carrier signal injection-based sensoreless control", in *Proc. IEEE APEC*, pp. 879-885, 2008.
- [16] D. Mingardi, M. Morandin, S. Bolognani, N. Bianchi, "On the properties of the differential cross-saturation inductance in synchronous machines", *IEEE Trans. Ind. Appl.*, vol. 53, no. 2, pp. 991-1000, Mar./Apr. 2017.
- [17] A. Vagati, M. Pastorelli, F. Scapino, G. Franceschini, "Impact of cross-saturation inductance in synchronous reluctance motors of the trasverse-laminated type", *IEEE Trans. Ind. Appl.*, vol. 36, no. 4, pp. 1039-1046, Jul./Aug. 2000.
- [18] M. Hinkkanen, P. Pescetto, S. E. Saarakkala, G. Pellegrino, R. Bojoi, "Sensorless self-commissioning of synchronous reluctance motors at standstill without rotor locking", *IEEE Trans. Ind. Appl.*, vol. 53, no. 3, pp. 2120-2129, May 2017.
- [19] Z. Qu, T. Tuovinen, M. Hinkkanen, "Inclusion of magnetic saturation in dynamic models of synchronous reluctance motors", in *XXth Int. Conf. on Elec. Mach.*, vol. 53, no. 3, pp. 992-998, Sep. 2012.
- [20] H. Awan, Z. Song, S. E. Saarakkala, M. Hinkkanen, "Optimal torque control of synchronous motor drives: plug-and-play method", *IEEE Ener. Conv. Congr. and Expo.*, pp. 334-341, 2017.
-

- 
- [21] R. P. Brent "Algorithms for minimization without derivatives", Mineola, NY: Dover Publ., 2013.
- [22] M. J. D. Powell, "An efficient method for finding the minimum of a function of several variable without calculating derivatives", *The comput. J.*, vol. 7, no. 2, pp. 155-162, 1964.
- [23] M. Fontana, "Progetto ed analisi di motore sincrono a magneti permanenti interni a salienza inversa con ridotta oscillazione di coppia", *Tesi di laurea magistrale*, Universita' degli Studi di Padova, 2015-2016.
- [24] S. Bolognani, "Appunti del corso di azionamenti elettrici".